AFRL-ML-WP-TR-2006-4081

FUNDAMENTALS OF FRETTING APPLIED TO ANISOTROPIC MATERIALS

High-Temperature Fretting Fatigue of Single-Crystal Nickel

T.N. Farris and H. Murthy

Purdue University
School of Aeronautics and Astronautics
315 N. Grant Street
West Lafayette, IN 47907-2023

DECEMBER 2005

Final Report for 06 September 2002 – 01 December 2005

Approved for public release; distribution is unlimited.

STINFO COPY

MATERIALS AND MANUFACTURING DIRECTORATE
AIR FORCE RESEARCH LABORATORY
AIR FORCE MATERIEL COMMAND
WRIGHT-PATTERSON AIR FORCE BASE, OH 45433-7750

NOTICE

PAO Case Number: AFRL/WS 06-0247, 30 Jan 2006.

THIS TECHNICAL REPORT IS APPROVED FOR PUBLICATION.

//Signature//

JEFFREY R. CALCATERRA, Chief
Processing Section
Metals, Ceramics & NDE Division

//Signature//

ROLLIE DUTTON, Chief
Metals Branch
Metals, Ceramics & NDE Division

//Signature//

GERALD J. PETRAK, Asst Chief
Metals, Ceramics & NDE Division
Materials & Manufacturing Directorate

REPORT DOCUMENTATION PAGE	*Form Approved OMB No. 0704-0188*

1. REPORT DATE *(DD-MM-YY)*: December 2005

2. REPORT TYPE: Final

3. DATES COVERED *(From - To)*: 09/06/2002 – 12/01/2005

4. TITLE AND SUBTITLE
FUNDAMENTALS OF FRETTING APPLIED TO ANISOTROPIC MATERIALS
High-Temperature Fretting Fatigue of Single-Crystal Nickel

5a. CONTRACT NUMBER: F33615-02-1-5223

5b. GRANT NUMBER

5c. PROGRAM ELEMENT NUMBER: 61102F

5d. PROJECT NUMBER: 2306

5e. TASK NUMBER: AL

5f. WORK UNIT NUMBER: 5G

6. AUTHOR(S)
T.N. Farris and H. Murthy

7. PERFORMING ORGANIZATION NAME(S) AND ADDRESS(ES)
Purdue University
School of Aeronautics and Astronautics
315 N. Grant Street
West Lafayette, IN 47907-2023

8. PERFORMING ORGANIZATION REPORT NUMBER

9. SPONSORING/MONITORING AGENCY NAME(S) AND ADDRESS(ES)
Materials and Manufacturing Directorate
Air Force Research Laboratory
Air Force Materiel Command
Wright-Patterson AFB, OH 45433-7750

10. SPONSORING/MONITORING AGENCY ACRONYM(S): AFRL-ML-WP

11. SPONSORING/MONITORING AGENCY REPORT NUMBER(S): AFRL-ML-WP-TR-2006-4081

12. DISTRIBUTION/AVAILABILITY STATEMENT
Approved for public release; distribution is unlimited.

13. SUPPLEMENTARY NOTES
Report contains color.
PAO Case Number: AFRL/WS 06-0247, 30 January 2006.

14. ABSTRACT (*Maximum 200 words*)
The objective of this program was to determine the fatigue crack growth portion of the dissimilar fretting fatigue tests in order to improve the accuracy of the equivalent stress method used to predict the fretting fatigue lives for the single crystal nickel on INl00 attachment fatigue tests. These analyses will give further confidence in the ability to determine endurance limits for attachment fatigue issues associated with these advanced materials.

15. SUBJECT TERMS
Fretting Fatigue, single crystal nickel, turbine engines, attachment, contact, partial slip, superalloy

16. SECURITY CLASSIFICATION OF: a. REPORT	b. ABSTRACT	c. THIS PAGE	17. LIMITATION OF ABSTRACT:	18. NUMBER OF PAGES	19a. NAME OF RESPONSIBLE PERSON (Monitor) / 19b. TELEPHONE NUMBER *(Include Area Code)*
Unclassified	Unclassified	Unclassified	SAR	104	Jeffrey R. Calcaterra / N/A

Standard Form 298 (Rev. 8-98)
Prescribed by ANSI Std. Z39-18

TABLE OF CONTENTS

Page

LIST OF TABLES v

LIST OF FIGURES vi

ABSTRACT x

1 Introduction 1

1.1 Fretting Phenomenon 2

1.2 Thesis Overview 4

2 Elevated Temperature Testing 6

2.1 Fretting Fatigue Testing Setup 6

2.2 Motivation for Elevated Temperature Testing 8

2.3 Elevated Temperature Experimental Setup 9

2.3.1 Fretting Chassis 9

2.3.2 Elevated Temperature Characteristics of Rig 10

2.3.3 Application and Monitoring of Contact Loads 12

2.3.4 Data Acquisition 13

2.4 Simple Model of Elevated Temperature Fretting Fatigue Experiment . 15

2.5 Fretting Specimens and Pads 17

2.5.1 Geometry of Fretting Pads and Specimens 17

2.5.2 Profilometry of Pads 17

2.5.3 Alignment of Specimen and Pads 20

2.6 Experimental Procedure 21

3 Mechanics of Fretting Contacts between Dissimilar/Anisotropic Materials . 26

3.1 Introduction 26

3.2 Governing singular integral equations 27

3.3 Coefficient of friction and the slip function 30

Page

3.4 Fretting Contacts Between Dissimilar Materials 32
3.4.1 Numerical solution of the partial slip contact problem 32
3.4.2 Verification of numerical method through partial slip contact of dissimilar isotropic materials 38
3.4.3 Partial slip contact problems involving single crystal nickel superalloys 39
3.5 Sub-Surface Stresses 41
4 Friction Coefficient 45
4.1 Introduction 45
4.2 Procedure for Friction Coefficient Evaluation Tests 45
4.3 Evaluation of Slip Zone Friction Coefficient 49
5 Experimental Observations 51
5.1 Fractography 51
5.2 Determination of Material Principal Axes 52
6 Life Estimation 58
6.1 Lifing Approaches 58
6.1.1 Fracture Mechanics Approaches 58
6.1.2 Crack Analogue Approach 59
6.1.3 Stress Based Approaches 59
6.2 Stress Based Approach for Predicting Nucleation 60
6.2.1 Prediction of Uniaxial Fatigue Tests 61
6.3 Stressed Area Correction 66
6.4 Life Estimation of Laboratory Tests 67
6.4.1 Stress Analysis 67
6.4.2 Nucleation paramater evaluation and stress area correction . . 68
6.4.3 Estimation of Crack Propagation Lives 70
7 Conclusion and Future Work 81
LIST OF REFERENCES 82
VITA 87

LIST OF TABLES

Table — Page

2.1 Experimental conditions for High Temperature fretting fatigue experiments with SCN on IN100. (σ^t=stresses measured by top load cell, σ^b=stresses measured by bottom load cell). ^{s} stopped because of problems with data acquisition, ^{r} runout tests. 24

4.1 Experimental conditions for fretting tests run before applying increasing amplitude waveform and the average friction coefficient obtained after applying the waveform. Cylindrical pads of radius $178mm$ were used in these tests. 47

4.2 Experimental conditions for fretting tests run before applying increasing amplitude waveform and the average friction coefficient obtained after applying the waveform. Nominally flat pads of flat length $3.05mm$ and edge radii of $3.05mm$ were used in these tests. 48

5.1 Angles obtained from Lauè patterns and the CMM. All angles are in degrees. Please refer to Figures 5.4 and 5.2 for the details of the angles. 57

6.1 Curve fit values for different nucleation parameters. The curve fit was assumed to be of the form $Damageparameter = A(N)^{-b}$ 63

6.2 Calculated nucleation life parameters and estimated propagation lives for fretting tests 73

LIST OF FIGURES

Figure Page

2.1 Components of the fretting chassis. 7

2.2 Schematic of the elevated temperature fretting fatigue experiments. . 10

2.3 (a) Photograph of the elevated temperature fretting fatigue setup. (b) Schematic of different loads. P is the normal load applied using actuators. Experiment is controlled by feedback from top load cell which measures R. Bulk load, F, bottom is measured by another load cell at the bottom. $Q = 0.5 \times (F - R)$ is calculated from loads F and R. . . 11

2.4 Schematic of the experiment conducted to obtain the load transfer ratio. P'/P was found to be $\approx 95\%$. 13

2.5 A simple linear model of the rig. (a) Schematic of the rig with specimen and pad (Figure 2.3(b)) . (b) A simple linear spring model of the setup. The part of the specimen below contact acts as a spring of stiffness k_1 and the part above acts as spring of stiffness k_3. The diaphragms act as springs of stiffness k_2. 16

2.6 (a) Schematic of the specimen used in experiment. Note that only central 190 mm of the specimen is made of the single crystal nickel. Waspaloy tabs are inertia welded onto this section. (b) Schematic of pads used in the tests. A taper of 5^o is provided on the upper surface of the pad to wedge the pad into the grove made in pad holder block. The contact surface has a flat length of 3.05 mm with radii 3.05 mm at the edges. The radius is over 10^o, and then a flat surface is machined. 18

2.7 (a) Schematic showing the material principal axes with respect to the specimen. (b) Effect of the change in orientation of principal axes with respect to contact surface on the subsurface stresses. 19

2.8 Typical trace of pad profile as machined. The prescribed profile is also plotted for comparison. 19

2.9 Schematic of the pad alignment fixture. (a) Front view of pad alignment (b) Top view of pad alignment fixture. By adjusting the four screws the pad holder block can be translated along z-axis and rotated about y-axis with respect to the specimen. 20

Figure Page

3.1 (a) Schematic of two elastic bodies in partial slip contact. a_1 and a_2 denote the ends of the contact zone and b_1 and b_2 denote the end of the stick zones. (b) The evolution of the contact and stick zones and the 'slip lock' phenomenon that occurs during the incremental indentation of an elastic half space by a rigid surface. 28

3.2 Schematic of the numerical scheme used to evaluate the Cauchy singular integrals. The solid circles represent the nodal positions and the hollow circles represent the collocation points (located at the mid point between the adjacent nodes). 36

3.3 Stick zone size as a function of the coefficient of friction. The values of $\frac{b}{a}$ obtained by solving the coupled singular integral equations incrementally are in excellent agreement to those obtained by Spence using a self-similar analysis. 38

3.4 Contact Tractions when a rigid nominally flat surface is indenting a Ti-6Al-4V half-space. (a) $P = 2.63\ MN/m$, $Q = -0.5\mu P$, $\sigma_o = 69\ MPa$. (b) $P = 2.63\ MN/m$, $Q = -0.75\mu P$, $\sigma_o = 517\ MPa$. Note that the relative slip in the two slip zones is in opposite directions in (b) due to high value of bulk stress. 40

3.5 (a) Shear traction when a rigid nominally flat surface is indenting a SCN half-space . Material principal axes are coincident with coordinate axes of the problem. (b) Effect of orientation of the material principal axes on shear traction. ($\theta_z = 45^o$ implies the material principal axes are rotated by a 45^o angle about the out-of-plane axis (z-axis)). ($P = 2.63\ MN/m$, $Q = -0.5\mu P$, $\sigma_o = 69\ MPa$). 41

4.1 Increasing amplitude waveform applied to determine the average coefficient of friction. This waveform is applied after running a fretting test for a fixed number of cycles. 46

4.2 Extreme values of Q/P during the application of increasing amplitude waveform. 46

5.1 Fretting fatigue fracture surface 10X. Specimen ZOKKA. 51

5.2 Schematic of the angles measured by the CMM. θ_1 is the angle between the normal, OA, and the axis of the specimen. θ_2 is the angle between the projection of the normal in YZ plane, OB, and the y-axis. 52

5.3 SEM fractographs of fretting fatigue crack in ZOKKA specimen. . . . 53

Figure Page

5.4 (a) Lauè diffraction as produced by orienting x-rays along primary axis of specimen. (b) Schematic highlighting procedure of identifying secondary and tertiary material axis orientations. Note that the dotted lines represent planes of symmetry in the FCC construction of SCN. . 54

5.5 Laue Pattern of specimen $ZOKKA$ along <1 0 0> direction (specimen axis). Four planes of symmetry can be observed. 55

5.6 (a) Laue pattern of $ZOKKA$ along <0 1 1>. Only two planes of symmetry are visible. (b) Laue pattern of $ZOKKA$ along <0 1 0>. Four planes of symmetry are visible. 55

6.1 Comparison of uniaxial data and fretting data with different lifing parameters. 64

6.2 Comparison of uniaxial data and fretting data with different lifing parameters. 65

6.3 Effect of machining tolerances on the surface normal traction. The distance, x, is normalized with respect to the half contact length obtained from the analysis using prescribed profile. Normal force $P = 1.58MN/m$ 68

6.4 A schematic illustration of effect of slip on evaluation of damage parameter. 69

6.5 A schematic illustration of effect of slip on evaluation of stressed area. 70

6.6 Comparison of uniaxial data and fretting data with different lifing parameters - Socie's parameter. 71

6.7 Comparison of uniaxial data and fretting data with different lifing parameters - Findley's parameter. 71

6.8 Comparison of uniaxial data and fretting data with different lifing parameters - CCB parameter. 72

6.9 Comparison of uniaxial data and fretting data with different lifing parameters - σ_{eq} parameter. 72

6.10 Schematic of the assumptions made during propagation analysis. The stresses resolved along and perpendicular to the plane of fracture were assumed to be applied on a specimen with crack perpendicular to its axis. 74

6.11 Stress intensity factors for corner cracks with remote shear stress. The graph has been reproduced from Murakami (1987) 76

6.12 Octahedral fatigue crack growth data in terms of ΔK_{oct} parameter. The graph has been reproduced from Telesman & Ghosn (1996). . . . 77

Figure Page

6.13 Comparison of predicted total life with experimentally observed failure life - Socie's parameter. 78

6.14 Comparison of predicted total life with experimentally observed failure life - Findley's parameter. 78

6.15 Comparison of predicted total life with experimentally observed failure life - CCB parameter. 79

6.16 Comparison of predicted total life with experimentally observed failure life - σ_{eq} parameter. 79

ABSTRACT

Haradanahalli, Murthy N. Ph.D., Purdue University, August, 2004. Fretting Fatigue of Anisotropic Materials at Elevated Temperatures. Major Professor: Thomas N. Farris.

The purpose of this research is to develop an experimental procedure to characterize the contact between blade and disk in aircraft turbo-machinery and to develop a model to predict the life of components based on the contact conditions. An experimental setup has been developed to conduct fretting fatigue tests at 610^oC and fretting fatigue lives are characterized for the contacting pair of IN100 and single crystal nickel subjected to a range of loading conditions. A well characterized set of experiments have been conducted to obtain the friction coefficient in the slip zone. A robust quasi-analytical approach, based on solution to singular integral equations, has been used to analyze the contact stresses. Different multi-axial fatigue parameters have been investigated for their ability to predict the initiation life of the specimens. An estimation of crack propagation life was made using conventional fracture mechanics approaches, after making certain assumptions to simplify the problem. Total life was predicted using nucleation life from different parameters and propagation life from conventional fracture mechanics approach. These predicted lives were compared with experimentally observed failure lives. The quality of the comparison provides confidence in the notion that conventional life prediction tools can be used to assess fretting fatigue at elevated temperatures.

ACKNOWLEDGMENTS

I thank Professor T. N. Farris for his encouragement and guidance during my stay at Purdue University. I have learnt a lot from him during my stay at Purdue University. He has been a great influence on me both academically and personally. I thank the rest of my committee, Professor Alten Grandt, Jr., Professor C. T. Sun and Prof. S. Chandrasekhar for their valuable inputs which helped me in improving my knowledge and understanding. I will never forget whatever I learned from the courses, AAE554, AAE 552 and AAE654, which helped me a lot during my research. I would like to thank Dr. M. Okane for his help in developing the elevated temperature testing setup and also for the nice interaction I had during his stay at Purdue University. The analytical code developed by Rajeev T. Pakalapati was very useful in the analysis of the experiments. I would like to thank Daniel B. Garcia for the SEM micrographs and for helping me learn a little bit of materials aspect of my research. I would also like to thank my Bachelors thesis advisor Dr. K. Bhaskar for getting me interested in solid mechanics and for all the informative discussions that I had with him.

I would like to thank my friend and mentor Harish Ganapathy for all the things I learnt from him and for helping me settle down in the laboratory. He has been a great friend and a great influence on my personality. Many thanks to Chris Tieche for teaching me to operate the testing machine. I had some of my best times in the lab with Harish, Chris, Rajeev, Bence and Eddie. I wish Bence and Eddie had stayed back at Purdue for their PhD. I would have welcomed the oppurtunity to interact with them more. I would like to thank Rajeev and his wife Annapoorna for playing host to me whenever I rushed to Columbus for a change of place. I had some of the best food in my life at Columbus, courtesy Annapoorna. The discussions I had with Daniel Garcia introduced me to lots of new ideas. I will miss all the arguments I had in lab with Dan, John and Matt and of course the most important work of the day. I hope to meet John in India someday. I had fun working with George, Sriram and Narayan. I wish them good luck in their studies. I thank my former room-mates Balaji, Ganapathy, Govi, Rajan and Manoj for making my stay at Purdue University a pleasant one. All my friends at Purdue helped me have a pleasant stay at Purdue University. I would like to thank Linda Weybright for all the help and the coffee, cookies and donuts. I would also like to thank Linda Flack for her help and for her patience with me whenever I registered on the last day of registration. I would like to acknowledge the suggestions and help of Wayne Ewbank, Joe Zachary and Mike in improving the experimental setup and for helping me with machining. I will miss the coffee room chat in Linda Weybright's office. I also thank Dave Reagan and Ivan Ellis for their help. Thanks to Kris Davis and Toby Lamb from central machine shop for their prompt reply while machining the experimental setup from them.

I would like to thank my brothers, Raj and Ravi, who have been the greatest influence in my life and helped me to be what I am. Thank you for all my achievements.

This work was supported in part under University of Dayton Research Institute (UDRI) subcontracts to Purdue University as part of the United States Air Force (USAF) high-cycle fatigue (HCF) program and GE Aircraft Engines (GEAE).

1. Introduction

The purpose of this research is to develop an experimental procedure to characterize the contact between blade and disk in aircraft turbo-machinery and to develop a model to predict the life of components based on the contact conditions.

Fretting is a frictional contact phenomenon that leads to damage at the region of contact between two nominally-clamped surfaces subjected to cyclic tangential loads causing small relative oscillations with respect to each other. Fretting differs from the phenomenon of sliding contact due to the fact that the components do not move with respect to each other globally. The kinematic condition imposed on the contact surface is a mixed boundary condition. The contact surface is divided into a region of "stick", where there is no relative motion between the two bodies in contact, and to a region of micro-slip at the edges, where the shear traction is equal to friction coefficient times the normal traction, thus causing the two surfaces to have a small tangential displacement relative to each other.

The associated edge-of-contact stresses sometimes initiate and grow cracks in a phenomenon known as fretting fatigue. The aggressive damage mechanisms associated with fretting pose a palpable threat to the structural integrity of aerospace systems. From the nucleation of widespread fatigue damage in riveted lap joint structure to the initiation and rapid propagation of edge-of-contact cracks at the blade/disk pair in jet engines, the sharp near-surface gradients of stress associated with the partial slip of contacting surfaces can severely degrade the fatigue performance of critical structural elements and mechanical systems. This report details an effort designed to couple fundamental mechanics and tribological insight with material fatigue response to develop a predictive methodology for fretting failures at elevated temperatures representative of aircraft engine-turbine stages.

1.1 Fretting Phenomenon

The damaging process in a fretting contact is a result of wear, corrosion and fatigue driven by the cyclic stresses and micro-slip at the edge of contact. Fretting was first reported by Eden et al. (1911) in 1911, who found that brown oxide debris was formed in the steel grips of their fatigue machine in contact with a steel specimen. But it was not until 1927 that Tomlinson (1927) conducted the first investigation of the process and designed two machines to produce small amplitude rotational movement between two annuli, and an annulus and a flat. Usually, in most of the components, fatigue occurs in association with fretting. McDowell (1953) showed that the action of fretting and fatigue together was more dangerous, producing strength reduction factors of 2-5 or even greater.

Hurricks (1970) has presented a survey of the three-stage damage mechanism observed during fretting. The first stage involves removing the thin oxide layer covering the material surface through the mechanical wear caused due to micro-slip and the stress gradients. As the oxide layer degrades after first few cycles of loads, the underlying material of the contact surfaces begins to adhere, forming micro-welds (Waterhouse & Taylor 1971). This adhesive process causes the accumulation of wear debris between the contact surfaces. In support of this mechanism, an increase in the measured coefficient of friction during the first few hundred cycles of fretting contact has been observed by several researchers (Nishioka & Hirakawa 1969, Endo & Goto 1976, Hills et al. 1988). As the cycles accumulate, there is plastic deformation near the surface. This leads to additional wear promoting more oxide formation (Waterhouse 1972). This near-surface plastic deformation can lead to nucleation of cracks which can result in fatigue failure if the cracks penetrate into the bulk of the material. Fretting has been observed in a variety of contact problems like roller bearings, riveted lap-joints, dovetail notches of the turbine blades (Kalb 1991) and even in artificial hip joints (Waterhouse 1981). Fretting has been observed to reduce the expected fatigue life by an order of magnitude.

From preliminary studies, driving forces for crack nucleation and subsequent failure of components have been observed to be high stress gradients at the edge of contact and the wear due to relative motion in slip zones. These, in turn, are influenced by a number of factors including:

1. Manufacturing Aspects: Geometric profiles of the contacting surface and their manufacturing tolerances, heat treatment, residual stresses introduced during machining etc.

2. Material aspects: material properties including fatigue and fracture characteristics (influenced by some of the manufacturing aspects like heat treatment, residual stresses introduced etc. and operating conditions like temperature, humidity etc.)

3. Tribological aspects: Friction coefficient between the contacting bodies, wear occurring at the edges of contact, surface evolution due to wear etc.

4. Mechanical aspects: Loads acting on the contacting surfaces, interaction of loads and geometry with the contact tribology that generates the oscillating stress field

The myriad of factors involved in the fretting fatigue process prove efforts for modeling effects of individual factors to be anything but trivial. Literature has proposed that as many as fifty variables can affect the fretting process (Dobromirski 1992). The complications involved in such investigations generally lead the industrial sector to situation specific experiments where the geometry and load conditions of a specific application can be replicated as closely as possible. This allows for determination of a fretting fatigue life reduction factor and subsequent redesign of current components to enlist protection or prevention countermeasures aimed at alleviating the identified fretting threat. The majority of fretting fatigue experiments are performed for either the identification of this fretting fatigue life reduction factor or the evaluation and verification of the desired fretting protection/prevention scheme.

Though cost effective in the short term, such experimental investigations become less economically palatable as continued spending is made on reproduction of each practical situation in which evidence of fretting fatigue is observed. The redesign to resist fretting fatigue in each of these applications is also difficult because of an insufficient understanding of the fretting fatigue parameters themselves.

1.2 Thesis Overview

For ease of studies, it is necessary to reduce the vast number of factors into a smaller set that still retains all the necessary features of the actual application. This base configuration of essential factors provides the foundation for experimental investigation and analysis of the fretting phenomenon. The ensuing investigation uses the base configuration of a flat pad with rounded edges held in contact with a flat specimen by a constant normal load and subjected to a sinusoidal tangential load and an in-phase bulk load. The loads are controlled and monitored by a data acquisition system with feedback control. The experiments are conducted at a temperature of 610^oC, by using a furnace-like environment to represent the temperatures experienced by the blade-disk contacts in engines. Actual profile of the contacting pad is obtained using a surface profilometer. Materials were chosen to represent the materials used in aircraft engine-turbine stages (IN100 on single crystal nickel). Material properties (like elasticity modulus, Poisson's ratio, fatigue and fracture strength etc.) and interface properties (like friction coefficient, wear characteristics etc.) are the properties of the contacting materials and hence are dependent upon set of materials chosen. Afore mentioned base configuration was used for all the tests conducted at a temperature of 610^oC. Well characterized experiments were conducted to obtain the friction coefficient at the contact interface. The material principal axes of the single crystal (face centered cubic crystal) was determined by Laue diffraction setup.

The experiments were analyzed using a quasi-analytical solution of singular integral equations (SIE) representing the contact configuration (Rajeev & Farris 2002).

Different multi-axial fatigue parameters were investigated for their ability to predict the initiation life of the specimens. An estimation of crack propagation life was made using conventional fracture mechanics approaches, after making certain assumptions to simplify the problem. Total life was predicted using nucleation life from different parameters and propagation life from conventional fracture mechanics approach. These predicted lives were compared with experimentally observed failure lives.

2. Elevated Temperature Testing

2.1 Fretting Fatigue Testing Setup

Fretting experiments involve a large number of independent parameters such as normal and tangential contact loads, bulk loads and shape of the contacting pairs. The relationship between normal and tangential contact loads depends upon the friction coefficient which changes during the fatigue process. Fretting tests may be carried out in the full sliding regime or the partial slip regime. As highlighted by Hills (1994), it is very difficult to achieve a well controlled experiment using an external actuator due to the low displacement amplitudes involved. Therefore it is beneficial to utilize compliance of the specimen to generate necessary tangential load, as a bulk load is applied to the specimen. A bridge-type setup utilizing the compliance of the bridge or specimen or both to generate tangential force has been used extensively for experimentation. Hills (1994) propose clamping the specimen with a pair of pads held by a chassis.

A bridge-type setup based on mechanics similar to that proposed by Hills (1994) has been developed at Purdue University for room temperature fretting fatigue tests (McVeigh et al. 1999). The fretting chassis is a superstructure built onto a conventional servohydraulic fatigue machine that allows the generation of tangential loads that are in phase with the bulk load, while applying a nominally constant normal load. Figure 2.1 shows the components of fretting chassis schematically. **Stiff beam** provides the bulk of stiffness of the chassis. Pads rest on the top platform which also provided the means of application of the normal load. Normal load is applied via a pair of hydraulic actuators that transmit the load onto the top platform. The two pressure rods ensure that the pressure is applied symmetrically to the pads. Thin steel diaphragms offer little resistance to pressure loading, but offer a large resistance that

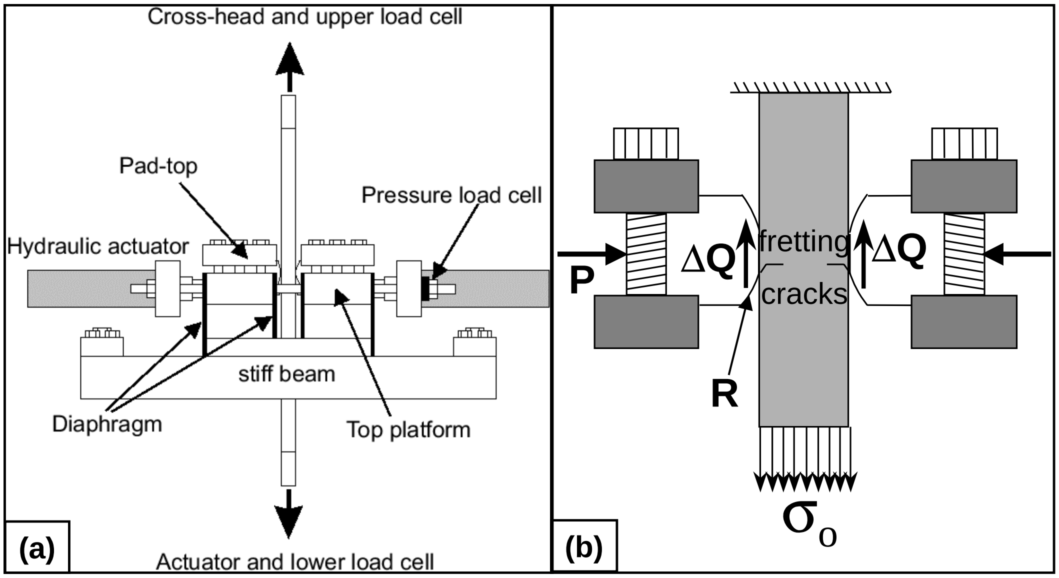

Figure 2.1. Components of the fretting chassis.

carries the portion of tangential load transmitted to the chassis. This ensures that almost all of pressure is transmitted to the specimen through pads, while maintaining the required stiffness to produce a large tangential force. Pad-tops fix the pads to the chassis. Tangential force produced is monitored throughout the fretting fatigue experiments, by recording the difference of the upper and lower load cell readings. With this setup, which utilizes a single actuator at the bottom, the tangential loads are in phase with the bulk loads.

Figure 2.1 shows a schematic of various loads that are relevant in the experiment. A number of sensors were used to keep track of the various parameters in the experiment. The experiments were conducted in load control with the controlling parameter being the load seen by the cross-head load cell (R). Load cell below the actuator measured the bulk load F. Tangential force, $2Q$, was given by the difference of the two load cell readings. Bulk stress, σ_o is simply F divided by the cross-sectional area of the specimen. Note that each experiment had two pads and the experiment was assumed to have a plane of symmetry. Two load washers connected to pressure rods measure the normal force, P. The fretting phenomenon arising due to combination of bulk loading on the specimen and normal and tangential loading applied by the pad was studied.

2.2 Motivation for Elevated Temperature Testing

The performance of a jet engine, measured in terms of thrust-to-weight ratio, can be increased by increasing turbine gas temperature and by reducing the weight of the engine using innovative designs and advanced materials. These materials have to be lighter and must have good structural integrity at high temperatures. The allowable metal temperature was very low in the earlier jet engines that had uncooled turbine blades cast from poly-crystalline nickel-based alloys. In recent years, a significantly improved turbine airfoil cooling design and use of cast directionally solidified turbine airfoils have increased the allowable turbine inlet gas temperature. As a result, higher thrust-to-weight ratio can be achieved in the engines. Anisotropic behavior and the elevated operating temperatures of these advanced materials pose significant problems for design and life prediction of advanced turbine blades. Fretting is one of the primary causes of HCF in turbine blades. Therefore, to characterize the effect of fretting on life of these components, experiments have to be conducted at operating temperatures of the materials in consideration and analysis has to include the effect of anisotropic behavior on the contact stresses.

Existing fretting rig at Purdue University had been designed to operate at room temperature. The rig was useful in testing the materials like Ti-6Al-4V, Ti17, and Inco718 that are used in components that operate at lower temperatures. However, advanced alloys like Single Crystal Nickel (SCN), IN100, etc. that are used in high temperature applications have characteristic properties at elevated temperature. Therefore, to study the material fretting fatigue characteristics, experiments must be conducted at elevated temperatures to which the material is exposed in engine environment. To achieve an elevated temperature of 610^{o}C at the contact region, a new rig was designed as is described next.

2.3 Elevated Temperature Experimental Setup

A 100 kN servo-hydraulic fatigue testing machine was used for all the experiments. A chassis was attached to the machine to hold pads in contact with the specimens. The chassis allows application of crushing load by the pad on the specimen and also acts as a spring to generate tangential forces. The specimen was gripped and loaded by the action of hydraulic actuators. Crushing loads were applied by chassis with the help of hydraulic actuator, the spring action of chassis producing the required tangential force. Elevated temperatures were obtained using igniters with on/off type of controller. A miniature furnace-type environment was created using ceramic paper and ceramic blocks.

2.3.1 Fretting Chassis

The fretting chassis is a superstructure built on the fatigue machine that allows the generation of tangential loads that are in phase with the bulk load, while applying a nominally constant normal load. Figure 2.2 shows the components of fretting chassis schematically. Components of the rig closer to the zone of elevated temperature were designed using Ti-6Al-4V alloy, while 4140 steel was used to design the components that were far away from the region of high temperature.

Load transfer in the new setup was based on a principle similar to that of the room temperature fretting setup. **Stiff beam** provides bulk of the stiffness of the chassis. Webs that form a part of the pad holder block act as membranes. These thin diaphragms ($thickness = 4.4\ mm$)transfer most of the normal load applied to it, but their stiffness in the tangential direction gives rise to tangential (shear) load at the contact which is eventually transmitted to the stiff beam. Normal load is applied via a pair of hydraulic actuators. Load washers attached to the two rods on either side of contact ensure that the pressure is applied symmetrically to pads while monitoring the applied normal load. This reduces any out-of-plane moments that could be generated during testing. Since the temperatures that would be encountered

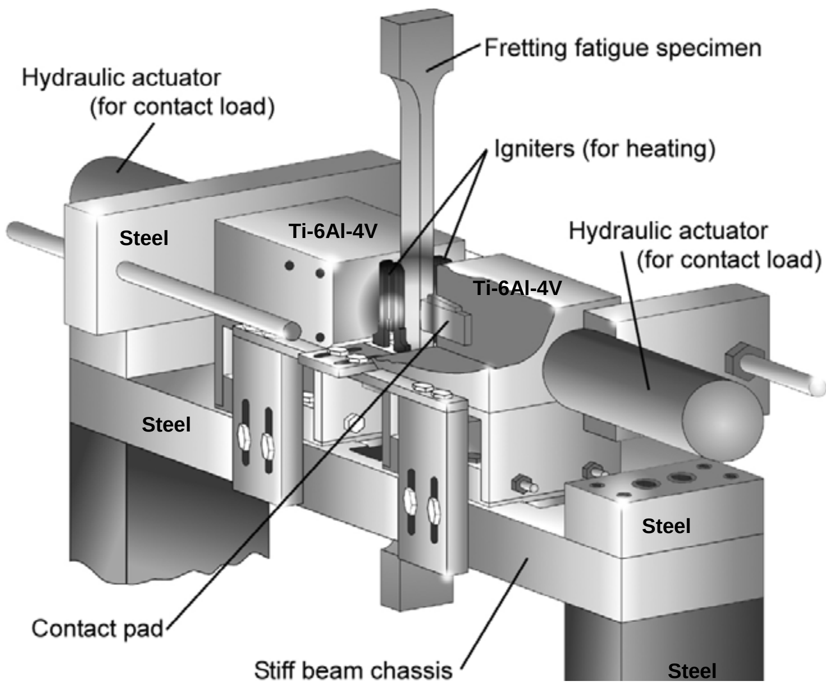

Figure 2.2. Schematic of the elevated temperature fretting fatigue experiments.

during the experiments were high, assembly of different parts using welds or bolts were avoided. Hence, the webs and platforms that hold the pads were machined from a single Ti-6Al-4V block. Further, the pad holder block was not made of two different parts that would be bolted together with pad in between them, as is done in the room temperature setup. As the normal load is applied, the pad gets wedged into a tapered groove (tapered at an angle of 5^o) machined in the pad holder block.

2.3.2 Elevated Temperature Characteristics of Rig

Temperature of the local area of contact was increased using a pair of igniters on either side of the specimen. Igniters draw a current of 4.25 A to 4.75 A at 132 V, and the maximum temperature achieved by igniter surface is 1550^oC. Heat transfer from the igniter to the specimen and the pads is through radiation and convection with air as the medium. Temperature of the specimen was measured using a K type thermocouple. Voltage output of the thermocouple was used to control the

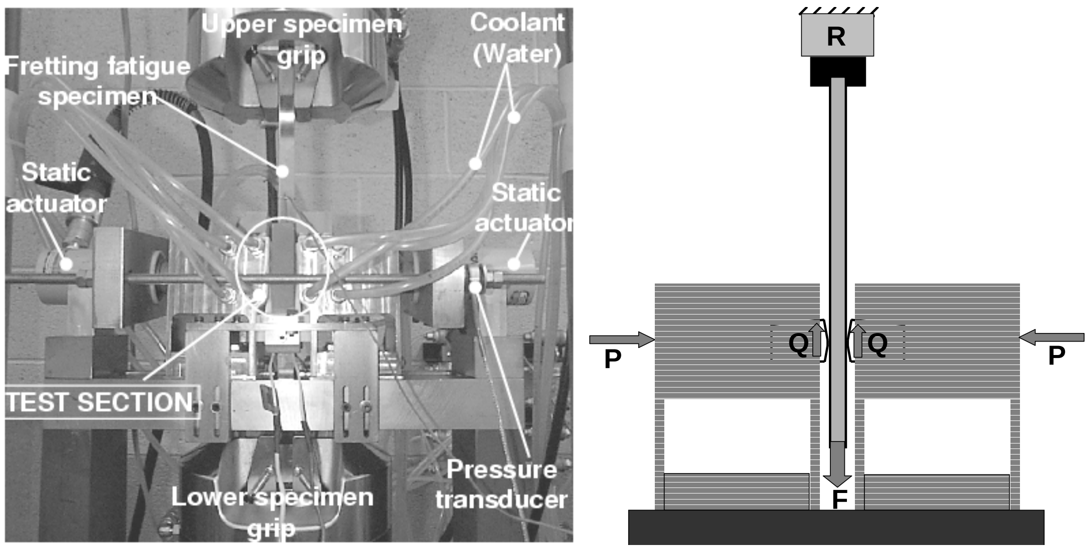

(a) (b)

Figure 2.3. (a) Photograph of the elevated temperature fretting fatigue setup. (b) Schematic of different loads. P is the normal load applied using actuators. Experiment is controlled by feedback from top load cell which measures R. Bulk load, F, bottom is measured by another load cell at the bottom. $Q = 0.5 \times (F - R)$ is calculated from loads F and R.

temperature at the contact using on/off control. The controller was set up such that the igniter switches off if temperature goes up by 1^{o}C from the desired temperature and switches on if the temperature drops by 0.5^{o}C. On/off control requires an igniter capable of reaching a very high temperature, in a short period of time, to minimize the fluctuations in temperature. Hence, an igniter which can achieve the maximum temperature from room temperature in 17 $secs$ was chosen. However, there was a fluctuation of $\pm 5^o C$ when the desired temperature was $610^o C$. The fluctuation may be due to air currents affecting the convective heat transfer, in addition to on/off type of control. The influence of air currents were minimized by forming a shield around the zone of elevated temperature, using ceramic blocks and sheets. Since the fluctuation was less than 1% of the desired value, it will be neglected in the subsequent modeling efforts.

Surface of the webs and the pad holder block facing the zone of elevated temperature was covered with ceramic sheets glued using high temperature adhesive, hence preventing their exposure to high temperatures. It also prevents absorption of heat by the rig from the elevated temperature zone. Loss of heat to ambient air was further prevented using a shield made of a ceramic block placed behind the igniter. Ceramic shields along with the ceramic sheets covering the rig give rise to a furnace-like environment around the region of contact. Inspite of covering the surface of webs with ceramic sheets, there is some heat transfer to the rig due to the air surrounding it which is at a very high temperature. In addition, there is a transfer of heat from the pad to the pad holder by conduction. To absorb the heat thus generated in the rig, the pad holders are cooled by passing water through channels machined in the block (Figure 2.3(a)). Heat is also conducted to the wedges that hold the specimens. Hence, water cooled wedges were used for clamping the specimens.

2.3.3 Application and Monitoring of Contact Loads

Figure 2.3(b) shows a schematic of the various loads that will be referred to in this document. P is the crush load (normal load), Q is the tangential load, F is the force applied at the bottom of the specimen (measured by the actuator load cell). The reaction force as measured by the cross-head load cell (top grip) is referred to as R.

The experiments were conducted in load control with the controlling parameter being the load seen by the cross-head load cell (R). The load cell near the bottom actuator measured the bulk load F. Tangential force, $2Q$, was given by the difference of the force measured by the two load cells. The bulk stress, σ_o is simply F divided by the cross-sectional area of the specimen. Note that each experiment had two pads and the experiment was assumed to have a plane of symmetry. Two load washers connected to the pressure rods measure the normal force and minimize out-of-plane moments. The cross-head load, position and cycle number were tracked via the digital

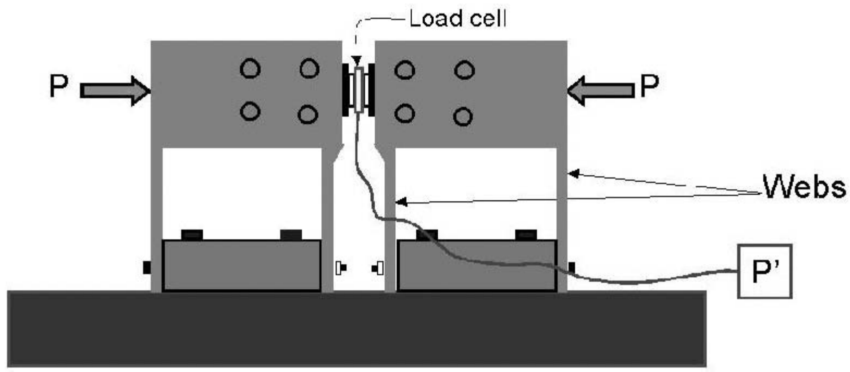

Figure 2.4. Schematic of the experiment conducted to obtain the load transfer ratio. P'/P was found to be $\approx 95\%$.

interface of the fatigue testing machine, while the rest of the sensors were monitored via a National Instruments SCXI module and data acquisition card. LabVIEW was used for control and data acquisition. The computer control allowed for the machine to run unattended.

A set of experiments were conducted to find the load transfer ratio when a normal load was applied (Figure 2.4). The load transfer ratio was found consistently to be between 94% and 96%. The experiments conducted to obtain the load transfer ratio also provided insight into techniques for minimizing the moment and rotation at the contact.

2.3.4 Data Acquisition

Since a fretting test involves collection of data over a large number of cycles, automated testing and data acquisition is necessary. Also, at each of the cycles, the number of measurements to be taken to characterize the conditions of fretting fatigue is large, which requires an efficient data acquisition system. The importance of the data acquisition has been documented by Attia (1992) in a summary of a series of papers aimed at developing a fretting fatigue test standard. Attia (1992) notes that measurement of contact parameters and automation of the testing procedure are areas to be addressed by the fretting fatigue community. Braun (1994) identifies the characteristics of an automated fatigue and fracture testing setup. The characteristics include: (1) a digital control system the implements the control loop and function generation for the waveform applied by the servo-hydraulic load frame via software, (2) a flexible data acquisition scheme allowing for a wide variety of experimental configurations and (3) an intuitive software-based user interface that relies on a graphical-user interface. The experimental setup for the fretting tests uses commercially available hardware components and software packages for an efficient, flexible and graphic oriented data acquisition system and on-line data processing. An Instron $100\,kN$ servo-hydraulic load frame, fitted with hydraulic wedge grips, applies the required fatigue loading of the specimen. An Instron 8500 digital controller sends the requisite signals to the servo valves to apply the load of particular frequency, waveform and amplitude. This controller can operate as a stand-alone controller through an attached panel or remotely through a digital input/output line that relies on a standardized general purpose interface bus (GPIB). This GPIB connection allows for integration of the controller with the standard PC bus architecture.

The load cells measuring the loads require full-bride Wheatstone circuits constructed on a printed circuit board. The excitation of each of these bridges and subsequent conditioning of the analog signals from the sensors is achieved with a general-purpose Signal Conditioning eXtensions for Instrumentation chassis (SCXI) manufactured by National Instruments. The module allows for user-definable excitation voltages (3.333 or 10 V), two-stage signal gains (from 1 to 1000) and two-stage filters (4Hz or 10 kHz). The current configuration offers up to eight channels, with the potential for expansion to twelve. The preconditioned analog signals from the array of sensors are then read from the SCXI chassis in either a multiplexed or parallel mode by a 16-bit analog-to-digital (A/D) data acquisition card in the PC. This card, an AT-MIO-16FE card also manufactured by National Instruments, can read up to 16 single-ended or 8 differential channels at a maximum of 20 kilosamples/second and a maximum resolution of 3 mV. It is completely software-configurable, complying with the latest *Plug and Play* hardware standards. This software configuration thus eliminates the need for cumbersome hardware jumper adjustments for varied experimental configurations. The real strength of this experimental setup lies in the ability for the hardware to be integrated into a single suite of user-friendly GUI panels that allow for the on-line control, monitoring and analysis of each fatigue experiment. This software platform has been developed using National Instrument's LabVIEW (the Laboratory Virtual Instrument Engineering Workbench package for Microsoft Windows). Since many of the base level operations such as direct communication with the DAQ hardware, generation of complex GUI's and data file creation and management are inherent parts of the LabVIEW subroutines, the time required to develop flexible, powerful software platforms for large-scale experimental setups is slashed. This is in tune with the current trend in using Supervisory Control and Data Acquisition (SCADA) as primary user-interface. LabVIEW falls under the purview of SCADA.

2.4 Simple Model of Elevated Temperature Fretting Fatigue Experiment

A simple model was developed, assuming that the specimen and the diaphragms act as linear springs, to assess the effects of various parameters on the nature of mixed-mode fretting process (Figure 2.5).

Portion of the specimen between the contact and the bottom grips acts as a spring of stiffness $k_1 = A_s E_s / l_1$, where A_s is the area of cross-section of the specimen, E_s is the Young's modulus of the specimen material and l_1 is the length of the specimen below contact. Similarly, portion of the specimen above contact acts as a spring of stiffness $k_3 = A_s E_s / l_3$, where l_3 is the length of the specimen between contact and the top grips. The two diaphragms act as springs of stiffness $k_2 = A_d E_d / l_d$, where A_d is the area of cross-section of the diaphragm, E_d is the Young's modulus of the diaphragm material and l_d is the length of the diaphragm. Though the assumption of linear spring behavior is not entirely accurate, it provides a qualitative assessment of the effect of the dimensions and material properties of the rig.

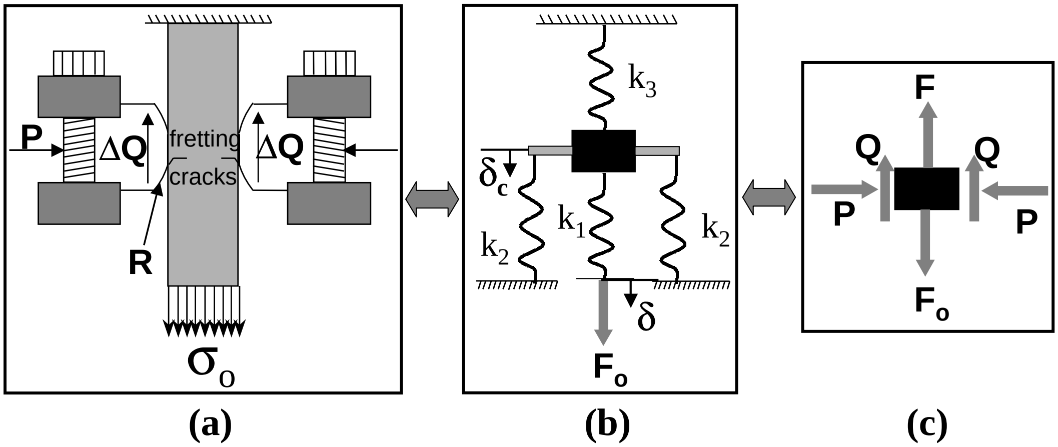

Figure 2.5. A simple linear model of the rig. (a) Schematic of the rig with specimen and pad (Figure 2.3(b)) . (b) A simple linear spring model of the setup. The part of the specimen below contact acts as a spring of stiffness k_1 and the part above acts as spring of stiffness k_3. The diaphragms act as springs of stiffness k_2.

The displacement at the bottom grip, where load F_o is applied, is taken as δ and the displacement at the contact is taken as δ_c. The forces can be related to the displacements as,

$$F_o = k_1(\delta - \delta_c), \quad F = k_3\delta_c, \quad Q = k_2\delta_c. \tag{2.1}$$

From above relations and from the equilibrium condition $F_o = F + 2Q$, the following relations can be deduced,

$$F = \frac{F_o}{1 + 2\frac{k_2}{k_3}}, \quad Q = \frac{F_o}{2 + \frac{k_3}{k_2}}. \tag{2.2}$$

Equation 2.2 gives a relation between the applied load, F_o, and the recorded loads, F and Q, in terms of the stiffnesses of the specimen and the diaphragms, which in turn are affected by the geometry and material properties. For example, if we want to decrease the Q/P ratio, we can do that by increasing k_3, i.e, by decreasing the length of specimen above the contact. This provided a valuable tool to modify the design as described in subsequent section.

2.5 Fretting Specimens and Pads

2.5.1 Geometry of Fretting Pads and Specimens

All specimens and pads were machined according to prescribed geometric specifications(Figure 2.6). The specimen is a 406.4 mm long dog-bone with a cross section of 15.2 mm x 9.5 mm. Cylindrical rods (200 mm long, 25.4 mm in diameter) cast from SCN were used to machine the fretting fatigue specimens. The primary principal axis (x_0) is possibly tilted from the cylinder axis (x_1) by a small angle ($< 10^o$). A rectangular cross section (15.2 $mm \times 9.5\, mm$) oriented at an arbitrary angle about the x_1-axis was machined. A schematic of the specimen orientation with respect to the material principal axes is shown in Figure 2.7(a). Tabs made from WASP alloy were inertia welded to the ends to produce the specimens. The nominally flat fretting pads were made from IN100. The pads were 20.3 mm high, 9.5 mm deep and had a prescribed profile of a 3.05 mm flat region bounded by 3.05 mm radii on either side. The specimens and pads were used as machined without any polishing. On the specimen, the contact is on the side with width 9.5 mm.

2.5.2 Profilometry of Pads

While the prescribed profile for the fretting pads was as is shown in Figure 2.6, the machined profiles were not in exact conformance with the prescribed profiles. Since the contact analysis using solution to singular integral equations (discussed later) are able to handle any arbitrary smooth profile, the machined profiles were recorded for each pad. A Talysurf profilometer was used to record a representative trace on each face of each pad used in the experiments. After centering and rotating, this trace was smoothened using a moving average approach and treated as the input to the stress analysis program discussed elsewhere in this report. Figure 2.8 shows a typical trace of the pad as machined. Also plotted is the prescribed profile and the smoothened profile used for contact stress analysis.

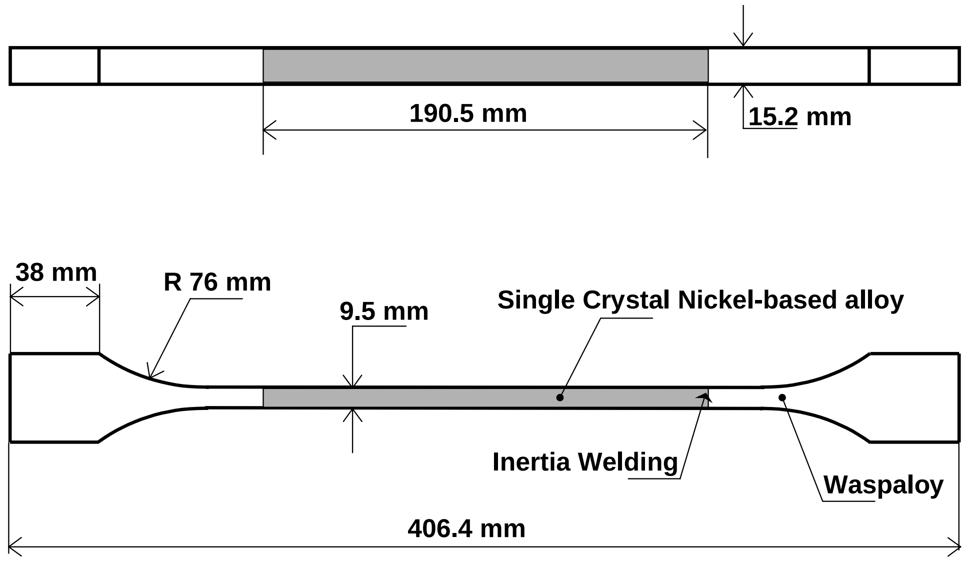

(a)

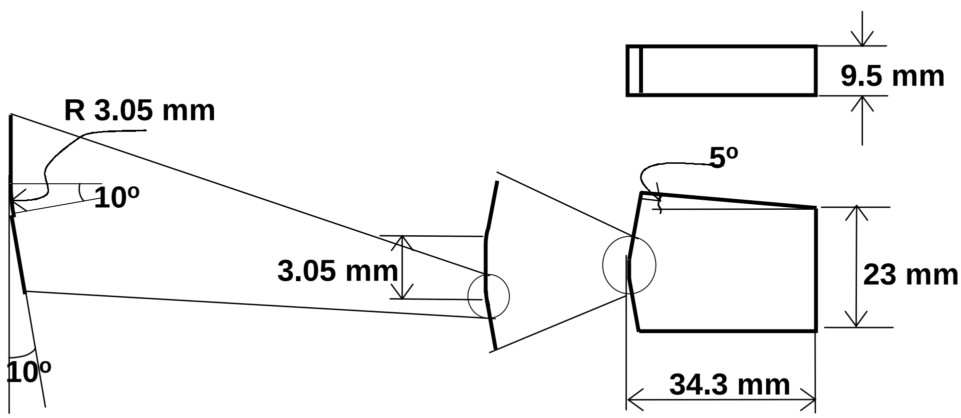

(b)

Figure 2.6. (a) Schematic of the specimen used in experiment. Note that only central 190 mm of the specimen is made of the single crystal nickel. Waspaloy tabs are inertia welded onto this section. (b) Schematic of pads used in the tests. A taper of 5^o is provided on the upper surface of the pad to wedge the pad into the grove made in pad holder block. The contact surface has a flat length of 3.05 mm with radii 3.05 mm at the edges. The radius is over 10^o, and then a flat surface is machined.

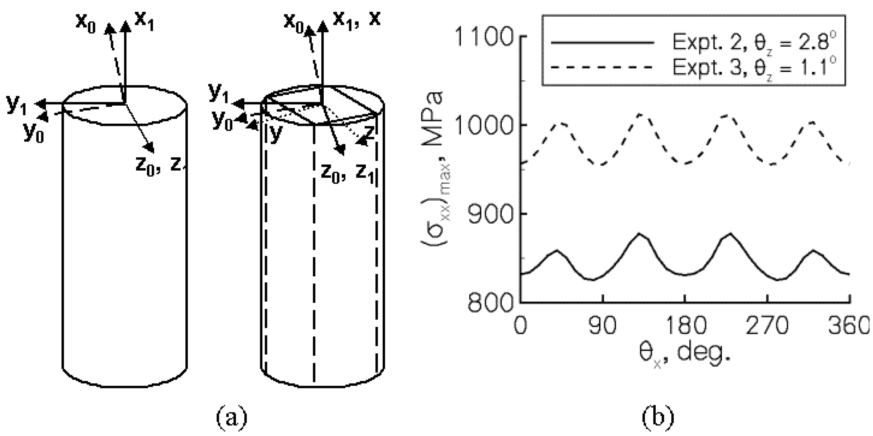

Figure 2.7. (a) Schematic showing the material principal axes with respect to the specimen. (b) Effect of the change in orientation of principal axes with respect to contact surface on the subsurface stresses.

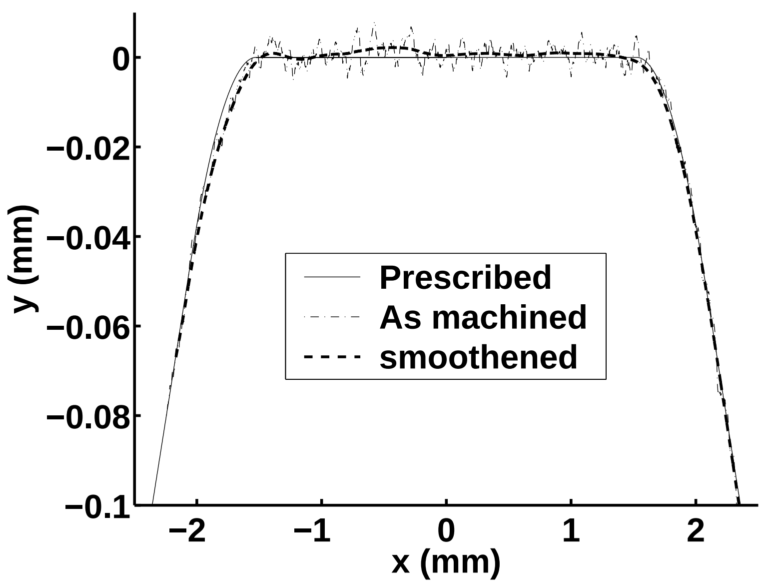

Figure 2.8. Typical trace of pad profile as machined. The prescribed profile is also plotted for comparison.

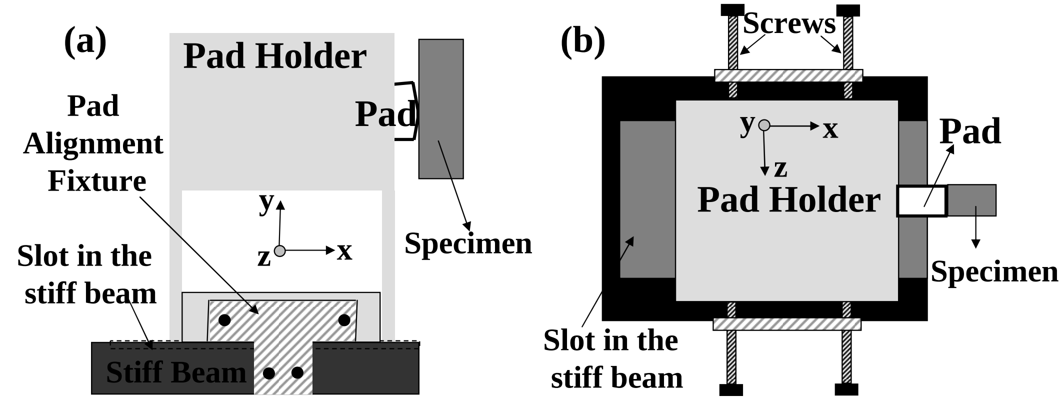

Figure 2.9. Schematic of the pad alignment fixture. (a) Front view of pad alignment (b) Top view of pad alignment fixture. By adjusting the four screws the pad holder block can be translated along z-axis and rotated about y-axis with respect to the specimen.

2.5.3 Alignment of Specimen and Pads

To ensure compliance with ASTM standards on specimen alignment for fatigue, an alignment specimen with eight strain gages was used. The strain gages were connected to four Wheatstone half-bridge circuits. By loading the specimen to a prescribed bulk load and adjusting the alignment fixture, the bending strain was minimized. This results in the minimization of the undesirable effects of the bending strains on the results. The bending strains, if significant, alter the fretting behavior to a great extent.

In addition, it was important to ensure that the pads were in proper contact with the specimen. Before applying the normal load, the pads were lightly pressed against the specimen, with a pressure sensitive film between the specimen and the pad. The color change on the film indicated the extent of contact. Adjustments were made to the fretting chassis and/or the machine to achieve full contact between the pads and the specimen. To aid the alignment of pad with respect to the specimen, an alignment fixture was designed (Figure 2.9). The alignment fixture was fixed firmly to the stiff beam. The pad holder block is kept in a slot in the stiff beam. The slot is slightly larger than the pad holder block, thus allowing for small amounts of translation and rotation in pad with respect to the specimen. The screws that are connected to the alignment fixture are then adjusted to translate (along z-axis) or rotate (about y-axis) the block and hence the pad with respect to the specimen. Once satisfactory contact was achieved, the pad holder block was firmly bolted onto the stiff beam and the full normal load was applied. The adequacy of this approach was borne out by observing the final wear scars that encompassed the contact zones.

2.6 Experimental Procedure

A procedure for setting up the experiment was arrived at based on the experience with the experiments conducted to estimate the load transfer ratio. This procedure was arrived at to minimize the moment and the rotation at the contact. First the pads are pushed into contact with the specimen by pushing the pad holder and held in place using screw-jacks. The pad holder moves towards the specimen in a groove in the stiff beam made of steel. The bolts holding the block on to the stiff beam chassis are tightened and the screw-jacks are removed. The small load applied at the bottom, using the screw-jacks, creates a moment about the contact. To relieve this moment, once a small normal load is applied using actuators, the bolts are loosened and tightened again. Finally, the normal load is applied using the hydraulic actuators. This causes the pad to get wedged into the groove in the pad holder. In the process of wedging, the pad moves into the groove. Hence, the webs now have to bend more while applying the normal load. This leads to a drop in load transfer ratio. To avoid the problem, the pad is pre-wedged into the grove by applying a normal load of about 110% of the normal load applied during the tests. The pre-wedging is achieved by applying increasing levels of normal load in three steps. At the end of each step, the rig is unloaded and the entire process of setting up the contact is repeated again. Normal load applied in the final step of pre-wedging is about 110% of the normal load applied during the tests.

As described, the normal load was applied first and allowed to settle. Then the mean of the bulk load was set. Finally, the cyclic load was applied at the given frequency. Note that since the load cell at the top is the controlling load cell, the cyclic load amplitude and mean at the top was set so as to provide the right steady state amplitude and mean of the bulk load. The tests were run at a frequency of $10\,Hz$, which was determined by the limitation of the fatigue testing machine.

Three preliminary experiments were conducted to understand the working of the rig and to study the nature of contact between the materials used at high temperatures. The details of the experiments are listed in Table 2.1. The first experiment provided valuable insight into the mechanics of the rig and the temperature variation at the contact. The temperature field was verified on the surface of the specimen by using multiple thermocouples. The variation was found to be 10^oC across the width of the specimen ($152.4\,mm$). Based on the behavior of the rig in the first experiment changes were made in the alignment procedure. The next two experiments served the purpose of verifying the working of the rig. Various lengths, discussed in the section on simple model of the rig, were such that the tangential load transferred to the pads caused the pad to slide against the specimen. The rig was designed with the intention of obtaining Q/P ratios of the order of $0.3-0.4$, based on previous experience with room temperature tests using Ti-6Al-4V specimens, wherein friction coefficient was $0.5-0.55$. However, during the contact between IN100 and single crystal nickel, coefficient of friction was found to be much lower($0.17-0.23$), due to which gross sliding (implying $Q=\mu P$) was observed during the course of experiments. Therefore, to achieve partial slip conditions, it is essential to alter the lengths such that much lower friction coefficients are achieved. In addition, it is possible that the relatively large displacements associated with sliding wear introduced non-linearity into the load transfer relationship. Thus, P could be smaller than the measured value. In order to alleviate these problems by achieving partial slip conditions representative of engine hardware, the tangential load has to be decreased such that $Q<\mu P$. From Equation 2.2, Q can be reduced either by increasing k_3 or by reducing k_2. Therefore, either the length of the specimen between the contact and the top grips could be reduced or the area of cross-section (i.e, the thickness) of the diaphragms could be reduced. The length of the specimen was reduced due to the ease of modification. This was achieved by raising the fretting chassis, relative to the specimen, using spacers. By this process, partial slip conditions were achieved in the subsequent experiments. Q/P ratios of up to 0.27 were achieved implying that the coefficient of friction could be higher than what was anticipated from the first few sliding experiments.

Subsequent tests were conducted under partial slip conditions to study the fretting phenomenon. The experimental conditions are listed in Table 2.1. Note that the controlling load is the load at the top. Hence, initially as the coefficient of friction was low, the tangential force was limited by the frictional force required to cause sliding of the pads against the specimen. As the coefficient of friction rose and reached a steady state, the tangential force stabilized resulting in the bulk load also stabilizing. Note that the quoted values of the loads refer to the stabilized values unless stated otherwise. As the forces stabilized, most of the experiments reached a state of partial slip, wherein the tangential force is not enough to cause gross sliding. This phenomenon of transition from sliding to partial slip is referred to as mixed-mode fretting. All the loads were monitored and stored for every cycle for the first few hundred cycles. Subsequently, data was stored at regular intervals (usually 100 cycles).

The fretting fatigue experiments were either run to failure, resulting in the specimens breaking in two, or till run-out, defined as 10^6 *cycles*. No failures were observed in the pads as can be expected, since there is no bulk load to propagate the initiated crack to failure. The specimens failed due to cracks initiated at the trailing edge of contact in all the failure tests. Contact stresses, which are highest at the edges of contact, drive the crack nucleation. The observation that crack nucleation occurred at all the edges of contact agrees with the idea that contact stresses drive crack nucleation. The cracks initiated at the bottom edge of contact failed since the bulk stresses are highest at the bottom. The bulk stresses are highest at the bottom as

Table 2.1. Experimental conditions for High Temperature fretting fatigue experiments with SCN on IN100. (σ^t=stresses measured by top load cell, σ^b=stresses measured by bottom load cell). ^{s} stopped because of problems with data acquisition, ^{r} runout tests.

Expt. No.	Controllable Loads			Measured Loads				Failure Life (cycles)
	P (kN/m)	σ^t_{max} (MPa)	σ^t_{min} (MPa)	σ^b_{max} (MPa)	σ^b_{min} (MPa)	Q_{max} (kN/m)	Q_{min} (kN/m)	
HTFF01	1873	212	52	323	4	853	-365	415,000^s
HTFF02	1852	400	53	442	14	315	-297	944,495
HTFF03	2193	290	78	358	23	519	-422	2,000,000^r
HTFF04	3345	401	89	533	14	1004	-569	174,973
HTFF05	3394	407	84	502	1	723	-634	169,815
HTFF06	3431	337	71	445	-1	821	-543	61,900
HTFF07	3466	369	100	441	2	550	-746	491,292
HTFF08	3659	363	60	476	1	863	-451	18,810
HTFF09	3373	312	58	469	32	1192	-202	16,044
HTFF10	3436	270	15	450	17	1372	15	21,800
HTFF11	3368	108	-62	302	1	1481	474	45,496
HTFF12	3446	170	2	311	11	1071	68	49,306
HTFF13	2729	192	19	312	8	912	-77	779,232
HTFF14	2482	287	20	480	10	1470	-74	37,528
HTFF15	2679	188	12	311	6	940	-48	29,616
HTFF16	2641	289	26	462	8	1315	-140	4,438
HTFF17	2680	179	3	313	11	1026	58	148,384
HTFF18	3262	123	-11	245	12	931	173	1,000,000^r
HTFF19	3358	178	41	242	7	489	-258	214,397
HTFF20	3382	164	-47	382	9	1664	430	33,105
HTFF21	3229	174	17	279	7	799	-78	1,000,000^r
HTFF22	3384	170	15	283	13	858	-14	1,670,000^r
HTFF23	3295	214	34	317	8	783	-203	48,473
HTFF24	2535	214	17	347	5	1010	-88	49,890
HTFF25	3255	159	-1	284	8	948	63	1,250,000^r
HTFF26	2453	242	44	347	9	800	-271	65,283

part of the bulk load at the bottom is transferred as the tangential load, Q, leading to a lower bulk stress at the top.

3. Mechanics of Fretting Contacts between Dissimilar/Anisotropic Materials

3.1 Introduction

When two solid bodies are in contact due to the action of external forces the resulting contact tractions are determined as a result of the following conditions: 1) the displacements of the two bodies are such that they are in contact in the contact zone, 2) the contact tractions on each body are in equilibrium with the applied loads (forces and moments) on that body, and 3) the contact tractions and displacements in the contact zone are consistent with the laws of friction.

Knowing the contact loads, bulk loads, friction coefficient and the profile of the contacting surfaces, contact stresses can be obtained either by a finite element analysis of the model (Kondoh & Mutoh 2000) or by solution to singular integral equations (SIEs) (Mindlin 1949, Jäger 1997, Rajeev & Farris 2002, Murthy et al. 2003). Several researchers have used analytical approaches to analyze problem of contact between half spaces of specific geometries (Mindlin 1949, Ciavarella et al. 1998, Goryacheva et al. 2002). Jäger (1997) has presented a general solution to singular integral equations (SIE) for the contact of polynomial surfaces subjected to combined normal and tangential loading. Hills et al. (1993) present a numerical analysis of fretting contact of a cylinder on flat geometry, taking into account the coupling between the contact pressure and shear traction caused by the material dissimilarities, for isotropic materials. Their method relies on Spence's (Spence 1973) solution to obtain the contact tractions due to the application of normal load alone; therefore, it is not easily extendable to indenters of varying geometries or to problems with more complex load histories. The problem of combined normal and tangential loading on a two dimensional (2-D) plane-strain contact between similar materials of arbitrary shapes, which are sufficiently flat in the vicinity of contact, has been solved using a very computationally efficient approach that accounts for the effect of bulk stress on the tractions (Murthy et al. 2003). Due to its computational efficiency, this approach based on solving a set of singular integral equations presents itself as a powerful design tool to analyze the effects of various factors like shape of the contact surface and load histories on crack nucleation. Experimental results are consistent with these efficient calculations (Murthy et al. 2001). However, contact between dissimilar materials cannot be solved using a similar approach, due to the coupling between the normal and shear tractions. Therefore Rajeev & Farris (2002) obtained a solution for the coupled singular integral equations representing the dissimilar contact problem using a very different approach as detailed below.

3.2 Governing singular integral equations

Assume a given profile $H(x)$, of a pad in contact with a semi-infinite half-space. A force, P, and moment, M, are applied on the half-space (an equal and opposite force-moment pair acts on the pad). A schematic of two elastic bodies in contact is shown in Figure 3.1(a). Let the displacements in the x and y directions be given by ${}_iu_x$ and ${}_iu_y$ respectively ($i = 1, 2$). The relative slip between the two bodies, $s(x)$, and the initial gap function, $H(x)$, in the contact zone are related to the displacements as,

$$s(x) = {}_2u_x - {}_1u_x \tag{3.1}$$

$$H(x) + C_1 x = {}_2u_y - {}_1u_y + H_0 \tag{3.2}$$

where H_0 is a constant and C_1 is the rotation term. The Green's function for the surface displacements of an anisotropic half-space subject to a line force on the surface at $x = 0$ can be obtained using the Stroh formalism as (Ting 1996):

$$\boldsymbol{u} = \frac{1}{\pi}\mathrm{Im}\left[\mathbf{V}\,\boldsymbol{q}\ln(x)\right] \tag{3.3}$$

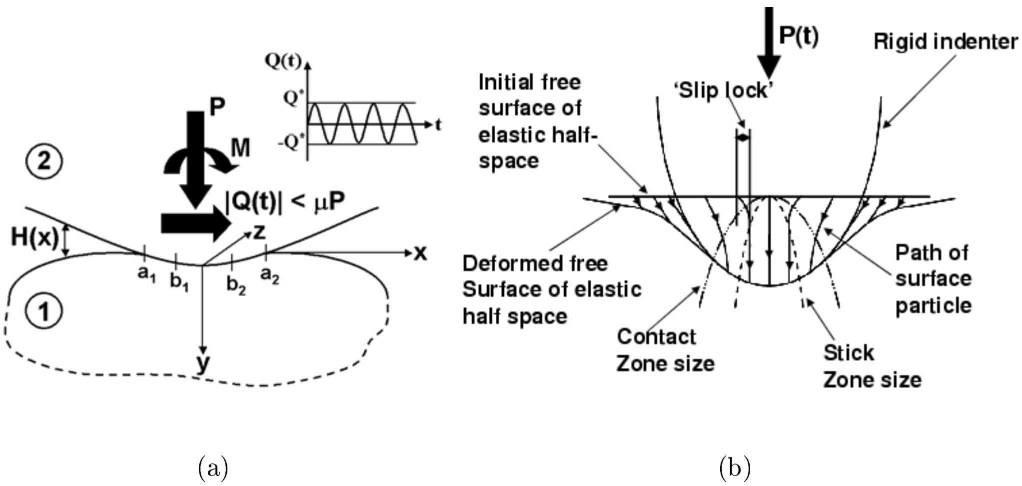

Figure 3.1. (a) Schematic of two elastic bodies in partial slip contact. a_1 and a_2 denote the ends of the contact zone and b_1 and b_2 denote the end of the stick zones. (b) The evolution of the contact and stick zones and the 'slip lock' phenomenon that occurs during the incremental indentation of an elastic half space by a rigid surface.

The constant matrices $\mathbf{V}_{3\times3}$ and $\boldsymbol{q}_{3\times1}$ are obtained from the elastic constants and the applied forces. From tensor C_{ijks} the following 3×3 matrices can be defined.

$$Q_{ik} = C_{i1k1}, \quad R_{ik} = C_{i1k2}, \quad T_{ik} = C_{i2k2} \tag{3.4}$$

The matrix $\mathbf{V} = [\boldsymbol{v}_1\, \boldsymbol{v}_2\, \boldsymbol{v}_3]$ is obtained from the eigenvalue problem:

$$\left[\mathbf{Q} + p(\mathbf{R} + \mathbf{R}^T) + p^2\mathbf{T}\right] \boldsymbol{v} = \mathbf{0} \tag{3.5}$$

It can be proved from strain energy considerations that the eigenvalues, p_i, and the eigenvectors, $\boldsymbol{v}_i$, are complex valued and hence occur in conjugate pairs. The matrix $\mathbf{V}$ is constructed using the eigenvectors corresponding to the eigenvalues with positive imaginary parts. The vector of constants $\boldsymbol{q}$ is given by:

$$\boldsymbol{q} = \mathbf{W}^{-1}\boldsymbol{f}, \quad \mathbf{W} = [\boldsymbol{w}_1\, \boldsymbol{w}_2\, \boldsymbol{w}_3], \quad \{\boldsymbol{w}_i\} = [\mathbf{R}^T + p_i\mathbf{T}]\boldsymbol{v}_i \tag{3.6}$$

where $\boldsymbol{f}$ is the applied line force vector. Noting that x can be written as $x = |x|e^{i\pi}$ for $x < 0$, the surface displacements due to an applied line force can be written as:

$$\boldsymbol{u} = \begin{cases} \mathrm{Re}[\mathbf{V}\mathbf{W}^{-1}]\,\boldsymbol{f} + \mathrm{Im}[\mathbf{V}\mathbf{W}^{-1}]\,\boldsymbol{f}\ln|x| & \text{if} \quad x < 0 \\ \mathrm{Im}[\mathbf{V}\mathbf{W}^{-1}]\,\boldsymbol{f}\ln|x| & \text{if} \quad x > 0 \end{cases} \tag{3.7}$$

Differentiating Equation 3.7 with respect to x,

$$\frac{\partial \boldsymbol{u}}{\partial x} = -\mathrm{Re}[\mathbf{V}\mathbf{W}^{-1}]\,\boldsymbol{f}\delta(x) + \mathrm{Im}[\mathbf{V}\mathbf{W}^{-1}]\,\boldsymbol{f}\frac{1}{x} \tag{3.8}$$

where $\delta(x)$ is Dirac's delta function. For distributed in-plane line tractions between $x = a_1$ and $x = a_2$ the surface displacements can be written as:

$$\frac{\partial}{\partial x}\left\{\begin{array}{c} u_x \\ u_y \end{array}\right\} = -\left[\begin{array}{cc} (\alpha_{11})_m & (\alpha_{12})_m \\ (\alpha_{21})_m & (\alpha_{22})_m \end{array}\right]\left\{\begin{array}{c} q(x) \\ p(x) \end{array}\right\} - \left[\begin{array}{cc} (\beta_{11})_m & (\beta_{12})_m \\ (\beta_{21})_m & (\beta_{22})_m \end{array}\right]\int_{a_1}^{a_2}\left\{\begin{array}{c} q(r) \\ p(r) \end{array}\right\}\frac{dr}{r-x} \tag{3.9}$$

where $(\alpha_{ij})_m = \mathrm{Re}[VW^{-1}]$ and $\beta_{ij} = \mathrm{Im}[VW^{-1}]$ for a given material m.

Considering that the tractions on the contacting bodies are equal and opposite in sign, Equation 3.9 can be written for both bodies with appropriate sign changes. By making use of Equations 3.1 and 3.2 the governing singular integral equations (SIEs) for 2-D contact problems can be written as,

$$\frac{\partial s}{\partial x} = \alpha_{11}q(x) + \frac{\beta_{11}}{\pi}\int_{a_1}^{a_2}\frac{q(r)}{r-x}\,dr + \alpha_{12}p(x) + \frac{\beta_{12}}{\pi}\int_{a_1}^{a_2}\frac{p(r)}{r-x}\,dr \tag{3.10}$$

$$\frac{\partial H}{\partial x} + C_1 = \alpha_{21}q(x) + \frac{\beta_{21}}{\pi}\int_{a_1}^{a_2}\frac{q(r)}{r-x}\,dr + \alpha_{22}p(x) + \frac{\beta_{22}}{\pi}\int_{a_1}^{a_2}\frac{p(r)}{r-x}\,dr \tag{3.11}$$

where the constants α_{ij} and β_{ij} are obtained from the elastic constants of the contacting bodies (Rajeev & Farris 2002). As an example when both the bodies are made from isotropic materials the non-zero constants are given by,

$$-\alpha_{21} = \alpha_{12} = \frac{(1-2\nu_2)(1+\nu_2)}{E_2} - \frac{(1-2\nu_1)(1+\nu_1)}{E_1} = k_1 \tag{3.12}$$

$$-\beta_{11} = -\beta_{22} = \frac{2(1-\nu_2^2)}{E_2} + \frac{2(1-\nu_1^2)}{E_1} = k_2 \tag{3.13}$$

where the subscripts 1 and 2 refer to bodies 1 and 2 respectively as shown in Figure 3.1. If one of the bodies, say body 1, is made from an anisotropic material and body 2 is made from an isotropic material, the constants in Equations 3.10 & 3.11 are given by:

$$[\boldsymbol{\alpha}] = \left[\begin{array}{cc} -(\alpha_{11})_1 & -\frac{(1-2\nu_2)(1+\nu_2)}{E_2} - (\alpha_{12})_1 \\ \frac{(1-2\nu_2)(1+\nu_2)}{E_2} + (\alpha_{21})_1 & -(\alpha_{22})_1 \end{array}\right] \tag{3.14}$$

$$[\boldsymbol{\beta}] = \left[\begin{array}{cc} -\frac{2(1-\nu_2^2)}{E_2} + (\beta_{11})_1 & (\beta_{12})_1 \\ (\beta_{21})_1 & -\frac{2(1-\nu_2^2)}{E_2} + (\beta_{22})_1 \end{array}\right] \tag{3.15}$$

As illustrated by Nowell & Hills (1987), in addition to the effect of normal and shear loads, it is essential to include the effect of remote stresses on surface tractions, as it can result in a reversal of slip direction for monotonic loading. The effect of remote stress on the contact tractions can be included by writing the slip function as,

$$s(x) = s_c(x) - \frac{(1-\nu^2)\sigma_0}{E}\,x \tag{3.16}$$

where $s_c(x)$ is the slip function due to the contact tractions alone.

If the initial gap function and the slip function are known, Equations 3.10 & 3.11 can be solved for the contact tractions. The initial gap function, $H(x)$, can be obtained from a knowledge of the undeformed geometry of the contacting bodies but the slip function, $s(x)$, is more complicated as it depends on load history.

3.3 Coefficient of friction and the slip function

Friction is the mechanism by which shear traction is transmitted between the contacting bodies. In the context of continuum mechanics, Coulomb's law of friction is most commonly used for contact problems. It states that when two bodies are clamped together under the action of a normal force, P, the shear force, Q, that is necessary to cause relative sliding of one body over the other is directly proportional to P. The direction of Q on a body and the direction of relative sliding of that body over the other are the same. The constant of proportionality is termed the coefficient of friction, μ. What happens when the shear force is not quite enough to induce gross relative sliding of the two contacting bodies? There are two possible answers: 1) there is no relative sliding between the contacting bodies, or 2) there is relative sliding in part of the contact region and no relative sliding in the remaining part. For isotropic materials Dundurs & Comninou (1979) deduced that, in order for Coulomb's law of friction to be satisfied at the edge of contact and for there not to be any inter-penetration of the contacting surfaces, there has to be some amount of relative sliding/slip between the contacting surfaces. This type of contact ($Q < \mu P$) is known as partial slip contact. Most commonly this is characterized by a central 'stick' zone in which no relative slip takes place surrounded by a 'slip' zone in which the tangential traction is limited by the available friction. These conditions, in a given load increment, can be written as,

$$\frac{\partial s(x,t)}{\partial t} = 0 \qquad x \in (b_1, b_2) \tag{3.17}$$

$$|q(x)| = \mu |p(x)| \quad x \in \{(a_1, b_1) \cup (b_2, a_2)\} \tag{3.18}$$

where b_1 and b_2 are the ends of the stick zone and a_1 and a_2 are the ends of the contact zone as shown in Figure 3.1(a).

If the next load increment at a given instant in time is such that the size of the stick zone grows into the slip zone then the accumulated slip in the newly added regions to the stick zone gets 'locked in'. This point is illustrated in Figure 3.1(b) for the case of normal indentation ($Q = 0$) of an elastic half space by a rigid punch. As the applied load, P, increases the point A on the surface of the half-space slips against the rigid surface until the stick zone extends to include that point. From that time onward any increase in the load does not result in additional slip. The slip is locked in. To solve Equations 3.10 & 3.11 for the contact tractions, knowledge of the accumulated slip function, $s(x,t)$, at the current instant of time is required. For the most general loading/unloading paths there is no way of knowing the slip function *a priori*. Hence Equations 3.10 & 3.11 have to be solved incrementally.

In the slip region the two contact surfaces slip against each other, Coulomb's law of friction calls for Equation 3.18 to be satisfied. This is ensured by writing the shear traction as,

$$q(x) = \mu f(x) p(x) - q^*(x) \tag{3.19}$$

where $f(x) = -1$ if the relative slip is in the same direction in both the slip zones and

$$f(x) = \begin{cases} 1 & \text{if} \quad x \in (a_1, b_1) \\ -\frac{2x}{b_2 - b_1} + \frac{b_2 + b_1}{b_2 - b_1} & \text{if} \quad x \in (b_1, b_2) \\ -1 & \text{if} \quad x \in (b_2, a_2) \end{cases} \tag{3.20}$$

if the relative slip is in opposite directions in the two slip zones. $q^*(x)$, usually called the 'corrective shear traction', is zero outside of the stick zone, and is such that $|q(x)| = |\mu f(x)p(x) - q^*(x)| < |\mu p(x)|$ within the stick zone ($b_1 < x < b_2$). Please note that $f(x) = -1$ implies that relative slip of body 2 over body 1 is in the direction of the negative x-axis for the axes shown in Figure 3.1(a) and $f(x)$ given by Equation 3.20 implies that body 1 is slipping outward relative to body 2. A reversal of these slip directions can be achieved numerically by reversing the sign of μ. Also, the friction law dictates that the shear traction in the slip zone (on body 1) be of the same sign as the relative slip. If this condition is not satisfied a different choice is made for $f(x)$ and/or the sign of μ.

3.4 Fretting Contacts Between Dissimilar Materials

3.4.1 Numerical solution of the partial slip contact problem

Substituting Equation 3.19 into Equations 3.10 & 3.11 the governing singular integral equations (SIEs) for the partial slip contact problem can be written as:

$$\begin{aligned}
\frac{\partial s}{\partial x} &= -\alpha_{11}q^*(x) - \frac{\beta_{11}}{\pi}\int_{b_1}^{b_2}\frac{q^*(r)}{r-x}\,dr + (\alpha_{12} + \mu f(x)\alpha_{11})p(x) \\
&\quad + \frac{(\beta_{12} - \mu\beta_{11})}{\pi}\int_{a_1}^{a_2}\frac{p(r)}{r-x}\,dr + \frac{\mu\beta_{11}}{\pi}\int_{a_1}^{b_2}\frac{(1+f(r))\,p(r)}{r-x}\,dr \qquad (3.21)\\
\frac{\partial H}{\partial x} + C_1 &= -\alpha_{21}q^*(x) - \frac{\beta_{21}}{\pi}\int_{b_1}^{b_2}\frac{q^*(r)}{r-x}\,dr + (\alpha_{22} + \mu f(x)\alpha_{21})p(x) \\
&\quad + \frac{(\beta_{22} - \mu\beta_{21})}{\pi}\int_{a_1}^{a_2}\frac{p(r)}{r-x}\,dr + \frac{\mu\beta_{21}}{\pi}\int_{a_1}^{b_2}\frac{(1+f(r))\,p(r)}{r-x}\,dr \qquad (3.22)
\end{aligned}$$

Equation 3.21 is applicable only in the stick zone ($b_1 < x < b_2$) whereas Equation 3.11 is applicable in the entire contact zone ($a_1 < x < a_2$). For an arbitrary choice of $\{a_1, a_2, b_1, b_2\}$ the solutions to Equations 3.21 & 3.22 will not be non-singular. Rajeev & Farris (2002) presented a numerical solution when both the bodies are made from dissimilar isotropic materials.

From the theory of singular integral equations (Muskhelishvili 1953, Gladwell 1980) it can shown that, depending on the type of behavior specified for $p(x)$, there are four different types of solutions possible. The pressure can be specified to be bounded at the ends of contact zone, singular at both ends, or bounded at one end and singular at the other. For contact of a smooth punch on an elastic half-space the pressure is required to be bounded at both the ends of the contact zone. This requires the following consistency condition to be satisfied:

$$\int_{a_1}^{a_2} \frac{\frac{\partial H}{\partial r} + C_1}{(r-a_1)^{1-A}(a_2-r)^A}\, dr = 0 \tag{3.23}$$

Also, in order to satisfy static equilibrium, $\int_{a_1}^{a_2} p(r)\, dr = P$ and $\int_{a_1}^{a_2} tp(r)\, dr = M$ where P & M are the applied normal load and moment respectively. For contact problems, in general, the ends of the contact zone are not known beforehand and Equation 3.23 may not be satisfied for an arbitrary choice of a_1 & a_2. To circumvent this problem a singularity is admitted in the function $p(x)$. Previous researchers (Karpenko 1966, Erdogan & Gupta 1972, Farris 1992, Kurtz et al. 1994) worked with the following representation of the pressure function to obtain a numerical solution of sliding contact problem

$$p(x) = \phi(x) \left(\frac{x-a_1}{a_2-x}\right)^{(1-A)} \tag{3.24}$$

where $\phi(x)$ was approximated using either piecewise continuous polynomials or as a sum of a finite number of polynomials. Thereafter, Equations 3.21 & 3.22 reduced to a set of linear equations by allowing it to be exactly satisfied at a discrete number of collocation points which can be solved to obtain either the values of $\phi(x)$ at the collocation points or the constant multipliers of the polynomial functions depending on the approximation used. The main problem applying a similar approach to this problem is that they cannot be extended to solve Equations 3.10 & 3.11 which have different domains of application, i.e., the initial gap function is known over the entire contact zone whereas the slip function is known only over the stick zone. This means that additional singularities have to be admitted at the stick/slip boundaries. A new method is required to handle these singularities. Therefore the following decomposition of the pressure function is considered,

$$p(x) = p_0(x) + \phi_1 \left(\frac{x-a_1}{a_2-x}\right)^{(1-A)} \tag{3.25}$$

where $p_0(x)$ is bounded, ϕ_1 is a constant, and A is obtained from Equation 3.23 as $\tan(\pi A) = -\left(\frac{\beta_{22}-\mu\beta_{21}}{\alpha_{22}-\mu\alpha_{21}}\right)$.

Just as was done for pressure (Equation 3.25) it is intuitive to write the corrective shear, $q^*(x)$, also in the same form,

$$q^*(x) = q_0^*(x) + \phi_2 \left(\frac{x-b_1}{b_2-x}\right)^B \tag{3.26}$$

where $q_0^*(x)$ is bounded in the entire stick zone. However when the above equation is substituted into Equation 3.22, a singularity arises at $x = b_2$. In order to cancel this singularity, since there is no singularity in the left hand side of Equation 3.22, consider the following form for the pressure function,

$$p(x) = p_0(x) + \phi_1 \left(\frac{x-a_1}{a_2-x}\right)^A + p_2(x) \tag{3.27}$$

where $p_0(x)$ is non-singular and $p_2(x)$ is given by:

$$p_2(x) = \begin{cases} 0 & \text{if} \quad x < b_1 \\ \phi_3 \left(\frac{x-b_1}{b_2-x}\right)^B & \text{if} \quad b_1 < x < b_2 \\ \phi_4 \left(\frac{a_2-x}{x-b_2}\right)^B & \text{if} \quad x > b_2 \end{cases} \tag{3.28}$$

The singularity index B has to be chosen such that the singularities in the right hand side of both the governing SIEs have to vanish.

By substituting Equations 3.27 & 3.26 into the RHS of Equation 3.21, the singular term, as $x \to b_2$ from the left, can be determined as,

$$\begin{aligned} S_1(x) \quad = \quad & \Big[\left(-\alpha_{11} + \beta_{11}\cot(\pi B)\right)(x-b_1)^B \phi_2 + \\ & + \left((\alpha_{12} - \mu\alpha_{11}) - (\beta_{12} - \mu\beta_{11})\cot(\pi B)\right)(x-b_1)^B \phi_3 \\ & + (\beta_{12} - \mu\beta_{11})\csc(\pi B)(a_2 - x)^B \phi_4\Big] \frac{1}{(b_2-x)^B} \end{aligned} \tag{3.29}$$

Similarly the singular terms in the RHS of Equation 3.22, as $x \to b_2$ from the left and the right, can be determined, respectively, as

$$\begin{aligned} S_2(x) \quad = \quad & \Big[(\beta_{21}\cot(\pi B) - \alpha_{21})(x-b_1)^B \phi_2 \\ & + \left((\alpha_{22}) - \mu\alpha_{21}) - (\beta_{22} - \mu\beta_{21})\cot(\pi B)\right)(x-b_1)^B \phi_3 \\ & + (\beta_{22} - \mu\beta_{21})\csc(\pi B)(a_2 - x)^B \phi_4\Big] \frac{1}{(b_2-x)^B} \end{aligned} \tag{3.30}$$

$$S_3(x) = \Big[\beta_{21}\csc(\pi B)(x-b_1)^B\phi_2 - (\beta_{22}-\mu\beta_{21})\csc(\pi B)(x-b_1)^B\phi_3 + ((\alpha_{22}-\mu\alpha_{21}) + (\beta_{22}-\mu\beta_{21})\cot(\pi B))(a_2-x)^B\phi_4\Big]\frac{1}{(x-b_2)^B} \tag{3.31}$$

These singularities can be made to vanish by setting $\lim_{x\to b_2^-}(b_2-x)^B S_{1,2}(x) = 0$ and $\lim_{x\to b_2^+}(x-b_2)^B S_3(x) = 0$. In matrix form these relations can be written as $[D(B)]\{\phi'\} = \{0\}$ where $\{\phi'\} = \{\ (b_2-b_1)^B\phi_2 \quad (b_2-b_1)^B\phi_3 \quad (a_2-b_2)^B\phi_4\ \}^T$. For a non-trivial solution of $\{\phi'\}$, $|D(B)| = \Delta(B) = 0$. By expanding $|D(B)|$ it can be determined that $\Delta(0) = -2(\beta_{22}-\mu\beta_{21})(\beta_{11}\beta_{22}-\beta_{21}\beta_{12}) = -\Delta(1)$. Hence there is at least one solution for B in the domain $0 < B < 1$. Also, by solving the eigenvalue problem, $[D(B)]\{\phi'\} = \{0\}$, ϕ_3 & ϕ_4 can be determined in terms of ϕ_2 and written in the form:

$$\phi_3 = \lambda_1\phi_2 \qquad \phi_4 = \lambda_2\phi_2 \tag{3.32}$$

As an example, consider the partial slip contact of dissimilar isotropic materials. The relevant material constants are given by Equations 3.12 & 3.13. The matrix $D(B)$ and its determinant, $\Delta(B)$, are given by:

$$D(B) = \begin{bmatrix} -k_2\cos(\pi B) & k_1\sin(\pi B) - \mu k_2\cos(\pi B) & \mu k_2 \\ k_1\sin(\pi B) & \mu k_1\sin(\pi B) + k_2\cos(\pi B) & -k_2 \\ 0 & -k_2 & \mu k_1\sin(\pi B) - k_2\cos(\pi B) \end{bmatrix} \tag{3.33}$$

$$\Delta(B) = -(k_2 + k_2^2\cos(\pi B) + k_1^2\sin(\pi B))(\mu k_1\sin(\pi B) - k_2\cos(\pi B)) \tag{3.34}$$

Therefore, the index of singularity, $B\,(0 < B < 1)$, at the right stick-slip boundary ($x = b_2$) during partial slip contact of dissimilar isotropic materials is given by $\cot(\pi B) = \frac{\mu k_1}{k_2}$. Dundurs & Comninou (1979) applied the William's eigen function expansion method to partial slip contact boundary conditions and obtained the same result. The constants ϕ_3 & ϕ_4 are given by

$$\phi_3 = 0 \tag{3.35}$$

$$\phi_4 = \left(\frac{b_2-b_1}{a_2-b_2}\right)^B \frac{\cos(\pi B)}{\mu}\phi_2 \tag{3.36}$$

$$\int_{a_1}^{a_2} \frac{p(r)}{r - x_j} dr = \sum_{1}^{N} \int_{r_i}^{r_{i+1}} \frac{p(r)}{r - x_j} dr$$

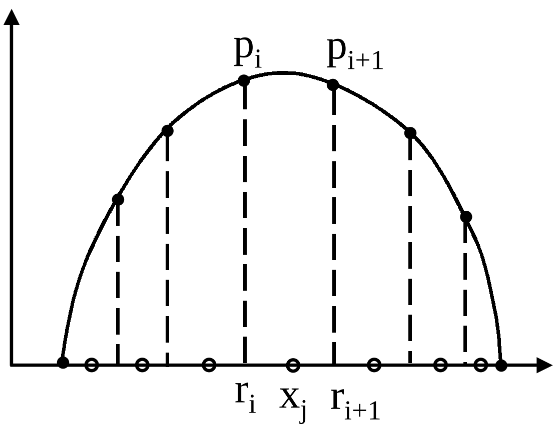

Figure 3.2. Schematic of the numerical scheme used to evaluate the Cauchy singular integrals. The solid circles represent the nodal positions and the hollow circles represent the collocation points (located at the mid point between the adjacent nodes).

A piecewise linear variation is assumed in between the nodes for $p_0(x)$. Equations 3.22 & 3.21 are reduced to a system of algebraic linear equations by enforcing it at a finite number of collocation points (not coincident with the node points). A schematic of the numerical procedure to evaluate the Cauchy singular integrals at the collocation points is shown in Figure 3.2. The contact region, $a_1 < x < a_2$, is divided into N elements. To facilitate easy implementation of the numerical code, the mesh is created such that the edges of the stick zone ($x = b_1$, b_2) always fall on node points. Let the number of elements in the stick zone be M.

We can use the following equations to discretize Equations 3.21 & 3.22 at the collocation points.

$$\begin{aligned}
\int_{a_1}^{a_2} \frac{f(r)p_0(r)}{r - x_j} dr &= \sum_{0}^{N} \int_{r_i}^{r_{i+1}} \frac{f(r)p_0(r)}{r - x_j} dr \\
&\approx \sum_{1}^{N} \left[\left\{ \left(1 - \frac{x_j}{r_{i+1} - r_i} \right) \log \left| \frac{r_{i+1} - x_j}{r_i - x_j} \right| - 1 \right\} f(r_i)\, p_i \right.
\end{aligned}$$

$$+ \quad \left\{ \frac{x_j}{r_{i+1} - r_i} \log \left| \frac{r_{i+1} - x_j}{r_i - x_j} \right| - 1 \right\} f(r_{i+1})\, p_{i+1} \Bigg] \quad (3.37)$$

where p_i & p_{i+1} are the values of $p_0(x)$ at the node points i & $i+1$ respectively and x_j is the j^{th} collocation point.

$$\int_{a_1}^{a_2} \left(\frac{r - a_1}{a_2 - r} \right)^A \frac{dr}{r - x} = \begin{cases} \pi \csc(\pi A) \left[1 - \left(\frac{a_1 - x}{a_2 - x} \right)^A \right] & \text{if} \quad x < a_1 \\ \pi \csc(\pi A) \left[1 - \cos(\pi A) \left(\frac{x - a_1}{a_2 - x} \right)^A \right] & \text{if} \quad a_1 < x < a_2 \\ \pi \csc(\pi A) \left[1 - \left(\frac{x - a_1}{x - a_2} \right)^A \right] & \text{if} \quad x > a_2 \end{cases} \quad (3.38)$$

This gives us a total of $N + M$ linear algebraic equations in $N + M + 4$ variables ($N+1$ values of $p_0(x)$, $M+1$ values of $q_0^*(x)$, ϕ_1, and ϕ_2). Four additional equations, $p_0(a_1) = p_0(a_2) = q_0^*(b_1) = q_0^*(b_2) = 0$, are used so that we may solve for the unknown contact pressure and the corrective shear traction.

The values for the edges of the contact zone (a_1, & a_2), the edges of the stick zone (b_1, & b_2), and the rotation of the punch, C_1, are obtained using an iteration scheme that is a modification of the Newton-Raphson method as applied to multi-variate problems. Let P_0, Q_0, and M_0 be the applied normal load, shear load, and moment respectively. To start with, the user inputs trial values for a_1, a_2, b_1, b_2, & C_1 and the iterations procedure is set in motion. In any given iteration, numerical integration (trapezoidal rule) is used to obtain loads due to the non-singular part of the tractions as,

$$P_i = \int_{a_{1i}}^{a_{2i}} p_{0i}(x)\, dx \quad (3.39)$$

$$Q_i = \int_{a_{1i}}^{a_{2i}} q_{0i}(x)\, dx \quad (3.40)$$

$$M_i = \int_{a_{1i}}^{a_{2i}} x p_{0i}(x)\, dx \quad (3.41)$$

where the subscript i refers to the values in the current iteration. If Equations 3.21 & 3.22 are solved again by changing one of the variables, say a_2, by a small amount, say Δa, then the following partial derivatives can be estimated numerically as: $\frac{\partial P}{\partial a_2} = \frac{\Delta P}{\Delta a}$, $\frac{\partial Q}{\partial a_2} = \frac{\Delta Q}{\Delta a}$, $\frac{\partial M}{\partial a_2} = \frac{\Delta M}{\Delta a}$, $\frac{\partial \phi_1}{\partial a_2} = \frac{\Delta \phi_1}{\Delta a}$, & $\frac{\partial \phi_2}{\partial a_2} = \frac{\Delta \phi_2}{\Delta a}$. Similarly, the partial derivatives of P,

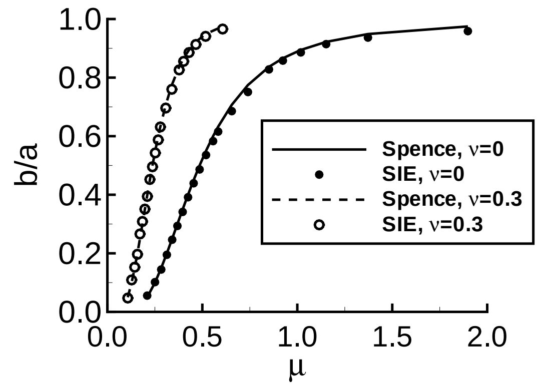

Figure 3.3. Stick zone size as a function of the coefficient of friction. The values of $\frac{b}{a}$ obtained by solving the coupled singular integral equations incrementally are in excellent agreement to those obtained by Spence using a self-similar analysis.

Q, M, ϕ_1, & ϕ_2 w.r.t $a_1, a_2, b_1, b_2,$ & C_1 are estimated numerically in each iteration. The next trial values are chosen as,

$$\left\{\begin{array}{c} a_1 \\ a_2 \\ b_1 \\ b_2 \\ C_1 \end{array}\right\}_{i+1} = \left\{\begin{array}{c} a_1 \\ a_2 \\ b_1 \\ b_2 \\ C_1 \end{array}\right\}_{i} + \left[\begin{array}{ccccc} \frac{\partial P}{\partial a_1} & \frac{\partial P}{\partial a_2} & \frac{\partial P}{\partial b_1} & \frac{\partial P}{\partial b_2} & \frac{\partial P}{\partial C_1} \\ \frac{\partial Q}{\partial a_1} & \frac{\partial Q}{\partial a_2} & \frac{\partial Q}{\partial b_1} & \frac{\partial Q}{\partial b_2} & \frac{\partial Q}{\partial C_1} \\ \frac{\partial M}{\partial a_1} & \frac{\partial M}{\partial a_2} & \frac{\partial M}{\partial b_1} & \frac{\partial M}{\partial b_2} & \frac{\partial M}{\partial C_1} \\ \frac{\partial \phi_1}{\partial a_1} & \frac{\partial \phi_1}{\partial a_2} & \frac{\partial \phi_1}{\partial b_1} & \frac{\partial \phi_1}{\partial b_2} & \frac{\partial \phi_1}{\partial C_1} \\ \frac{\partial \phi_2}{\partial a_1} & \frac{\partial \phi_2}{\partial a_2} & \frac{\partial \phi_2}{\partial b_1} & \frac{\partial \phi_2}{\partial b_2} & \frac{\partial \phi_2}{\partial C_1} \end{array}\right]^{-1} \left\{\begin{array}{c} P_0 - P_i \\ Q_0 - Q_i \\ M_0 - M_i \\ 0 - \phi_1 \\ 0 - \phi_2 \end{array}\right\} \qquad (3.42)$$

The iteration procedure is carried out until all the relevant quantities converge to a pre-specified tolerance. For some of the cases presented in this work the solution is not obtained within a pre-specified number of iterations. In such cases the program stops and prompts the user for new trial values of $a_1, a_2, b_1, b_2,$ & C_1.

3.4.2 Verification of numerical method through partial slip contact of dissimilar isotropic materials

Spence (1973) gives the contact tractions and the size of the stick zone when an elastic half space is indented by a rigid power law indenter ($H(x) \propto x^n$) under the influence of normal load alone ($Q = 0$). Under such conditions the solution is symmetric with respect to contact pressure and anti-symmetric with respect to the shear traction. Hence, the ends of the contact zone and the ends of the stick zone will be located symmetrically about the origin ($a_2 = -a_1 = a$ and $b_2 = -b_1 = b$). Exploiting the self-similarity of the problem, Spence reasoned that the ratio of the size of the stick zone to the size of the contact area remains fixed irrespective of the shape, given by the index n, of the power law indenter. Moreover, this ratio depends only on the Poisson's ratio (ν) of the half-space and the coefficient of friction (μ). The present analysis technique is applied to this problem by incrementally indenting an elastic half-space by a rigid parabolic punch ($n = 2$). The slip function in the very first increment is assumed to be zero within the stick zone. Results of this analysis are in good agreement with Spence's results implying that the numerical implementation is correct (Figure 3.3).

As the normal load increases the surface of the half-space slips against the rigid nominally flat indenter thereby producing an anti-symmetric shear traction (it has to integrate to zero) and is shown in Figure 3.4(a). Figure 3.4(a) also shows the shear traction after the simultaneous application of the shear load ($Q = -0.5\mu P$) and the remote tension ($\sigma_0 = 69\,\mathrm{MPa}$). The application of the remote tension tends to reduce the amount of relative slip in the left zone and increase it in the right slip zone. This effect can increase (with increasing σ_0) so much that relative slip in opposite directions is observed in both the slip zones as shown in Figure 3.4(b). As can be seen from Figures 3.4(a-b), the results obtained from the SIE analysis are in good agreement with the FE results (Rajeev & Farris 2002).

3.4.3 Partial slip contact problems involving single crystal nickel superalloys

Single crystal nickel superalloys (SCN) are orthotropic materials. For arbitrary orientation of the material principal axes, application of in-plane tractions on an orthotropic half-space might produce out-of-plane displacement. This phenomenon will cause relative slip between the two contacting bodies, and hence a shear traction

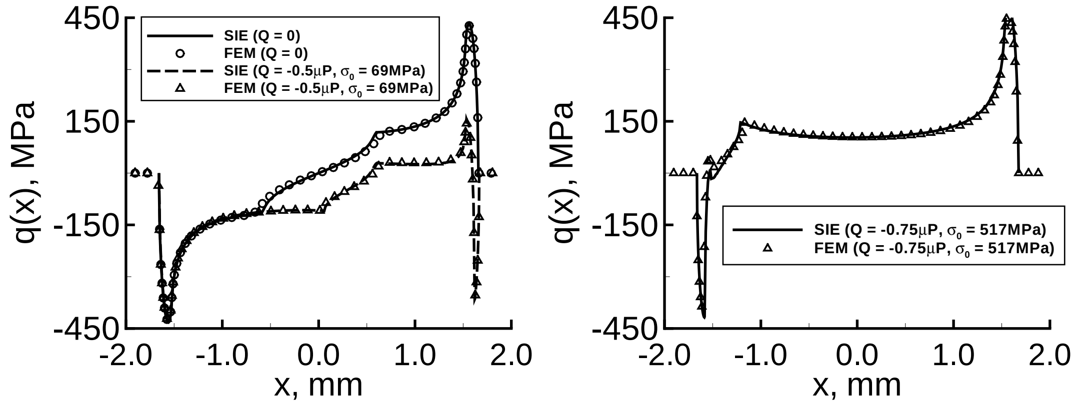

(a) (b)

Figure 3.4. Contact Tractions when a rigid nominally flat surface is indenting a Ti-6Al-4V half-space. (a) $P = 2.63\ MN/m$, $Q = -0.5\mu P$, $\sigma_o = 69\ MPa$. (b) $P = 2.63\ MN/m$, $Q = -0.75\mu P$, $\sigma_o = 517\ MPa$. Note that the relative slip in the two slip zones is in opposite directions in (b) due to high value of bulk stress.

at the contact interface in the out-of-plane direction. Incorporating this out-of-plane stick/slip behavior in the solution methodology would mean solving three coupled SIEs to obtain the contact tractions. As a means of simplifying the problem an "anisotropic" coefficient of friction is assumed ($\mu_x = \mu$ & $\mu_z = 0$). This way the out-of-plane shear traction can be identically set to zero and the number of coupled SIEs is reduced to two given by the system of Equations 3.21 & 3.22. This assumption is exact for orthotropic materials if the out-of-plane axis (z-axis) is one of the material principal axes as shown by Lekhnitskii (1981).

Verification of the SIE analysis is achieved by comparing its results with FE results. As with the isotropic case, a rigid nominally flat surface is first brought into contact with a SCN half-space under the action of normal load alone ($P = 2.63$ MN/m). Then a tangential force is applied ($Q = -0.5\mu P$) while simultaneously applying a remote tension ($\sigma_0 = 69$ MPa) to the half-space. The analysis is carried out for two different orientations of the material principal axes: 1) when they are coincident with the coordinate axes of the problem, and 2) when they are rotated 45^o about the out-

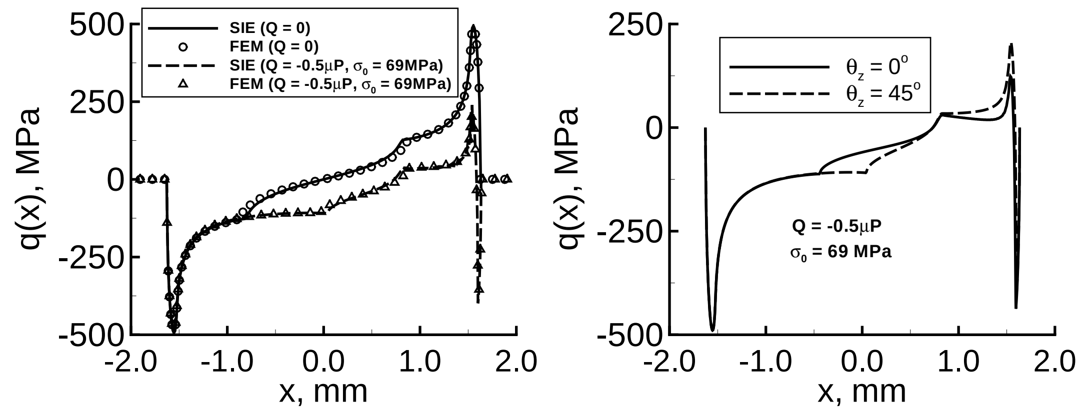

(a) (b)

Figure 3.5. (a) Shear traction when a rigid nominally flat surface is indenting a SCN half-space . Material principal axes are coincident with coordinate axes of the problem. (b) Effect of orientation of the material principal axes on shear traction. ($\theta_z = 45^o$ implies the material principal axes are rotated by a 45^o angle about the out-of-plane axis (z-axis)). ($P = 2.63\ MN/m$, $Q = -0.5\mu P$, $\sigma_o = 69\ MPa$).

plane-axis (z-axis). As can be seen from Figure 3.5(a), the SIE results are in good agreement with the FE results (Rajeev & Farris 2002). Figure 3.5(b) illustrates the effect of the orientation of the material principal axes on the shear traction.

3.5 Sub-Surface Stresses

If the displacement field is independent of z (the out-of-plane coordinate) then the strains and stresses will also be independent of z. Hence the three equilibrium conditions can be written as

$$\frac{\partial \sigma_{xx}}{\partial x} + \frac{\partial \sigma_{xy}}{\partial y} = 0 \quad (3.43)$$

$$\frac{\partial \sigma_{xy}}{\partial x} + \frac{\partial \sigma_{yy}}{\partial y} = 0 \quad (3.44)$$

$$\frac{\partial \sigma_{zx}}{\partial x} + \frac{\partial \sigma_{yz}}{\partial y} = 0 \quad (3.45)$$

For a linear elastic material the stress-strain relationship can be written as

$$\{\sigma\} = [C]\{\epsilon\} \tag{3.46}$$

and the strain-displacement can be written as

$$\{\epsilon\}^T = \left\{ \frac{\partial u}{\partial x} \quad \frac{\partial v}{\partial y} \quad 0 \quad \frac{\partial w}{\partial y} \quad \frac{\partial w}{\partial x} \quad \frac{\partial u}{\partial y} + \frac{\partial v}{\partial x} \right\} \tag{3.47}$$

where u, v, and w are the displacements in the x, y, and z directions respectively. Since substituting Equations 3.46 & 3.47 into Equations 3.43-3.44 will result in a system of linear homogeneous partial differential equation of the second order, the method of Fourier transforms can be used very effectively to solve for the sub-surface stress, strains, and displacements. Basically the displacements are written as

$$\{u(x,y) \;\; v(x,y) \;\; w(x,y)\} = \{\hat{u}(\omega,\eta) \;\; \hat{v}(\omega,\eta) \;\; \hat{w}(\omega,\eta)\} e^{i\omega x} e^{i\eta y} \tag{3.48}$$

Making use of Equations 3.43-3.48 it can be deduced that the following relationship must hold.

$$[\Lambda] \left\{ \begin{array}{c} \hat{u} \\ \hat{v} \\ \hat{w} \end{array} \right\} = \left\{ \begin{array}{c} 0 \\ 0 \\ 0 \end{array} \right\} \tag{3.49}$$

$$\Lambda_{11} = C_{66}k^2 + 2C_{16}k + C_{11} \tag{3.50}$$

$$\Lambda_{12} = C_{26}k^2 + (C_{12} + C_{66})k + C_{16} \tag{3.51}$$

$$\Lambda_{13} = C_{46}k^2 + (C_{14} + C_{56})k + C_{15} \tag{3.52}$$

$$\Lambda_{21} = C_{26}k^2 + (C_{66} + C_{12})k + C_{16} \tag{3.53}$$

$$\Lambda_{22} = C_{22}k^2 + 2C_{26}k + C_{66} \tag{3.54}$$

$$\Lambda_{23} = C_{24}k^2 + (C_{46} + C_{25})k + C_{56} \tag{3.55}$$

$$\Lambda_{31} = C_{46}k^2 + (C_{56} + C_{14})k + C_{15} \tag{3.56}$$

$$\Lambda_{32} = C_{24}k^2 + (C_{46} + C_{25})k + C_{56} \tag{3.57}$$

$$\Lambda_{33} = C_{44}k^2 + 2C_{45}k + C_{55} \tag{3.58}$$

where C_{ij} are the elastic constants and $k = \frac{\eta}{\omega}$. For a non-trivial solution of Equation 3.49 the determinant of the matrix Λ must be equal to zero. Setting $|\Lambda| = 0$ gives us three complex conjugate pairs of eigenvalues. To ensure that the stresses, strains, and displacements are bounded as $y \to \infty$ only the roots with positive real parts are chosen to write down the solution for a positive value of ω. We will first present the solution method when the eigenvalues are distinct (SCN falls under this category).

Let E_i be the eigenvector corresponding to the eigenvalue λ_i, and let c_1, c_2, and c_3 be the constant multipliers of the three principal solutions. The displacement solution for a particular frequency, ω, is given by

$$\left\{ \begin{array}{c} u \\ v \\ w \end{array} \right\} = [E] \left\{ \begin{array}{c} c_1 e^{i\lambda_1 \omega y} \\ c_2 e^{i\lambda_2 \omega y} \\ c_3 e^{i\lambda_3 \omega y} \end{array} \right\} e^{i\omega x} \tag{3.59}$$

where $E = [E_1 \;\; E_2 \;\; E_3]$. Substituting Equation 3.59 into Equation 3.47 we get, for the strain solution,

$$\begin{aligned} \{\epsilon\} &= \begin{bmatrix} E_{11} & E_{12} & E_{13} \\ E_{21}\lambda_1 & E_{22}\lambda_2 & E_{23}\lambda_3 \\ 0 & 0 & 0 \\ E_{31}\lambda_1 & E_{32}\lambda_2 & E_{33}\lambda_3 \\ E_{31} & E_{32} & E_{33} \\ E_{11}\lambda_1 + E_{21} & E_{12}\lambda_2 + E_{22} & E_{13}\lambda_3 + E_{23} \end{bmatrix} \left\{ \begin{array}{c} c_1 e^{i\lambda_1 \omega y} \\ c_2 e^{i\lambda_2 \omega y} \\ c_3 e^{i\lambda_3 \omega y} \end{array} \right\} (i\omega)\, e^{i\omega x} \\ &= [B] \left\{ \begin{array}{c} c_1 e^{i\lambda_1 \omega y} \\ c_2 e^{i\lambda_2 \omega y} \\ c_3 e^{i\lambda_3 \omega y} \end{array} \right\} (i\omega)\, e^{i\omega x} \end{aligned} \tag{3.60}$$

Please note that in the above equation E_{ij} refers to the $(i,j)^{th}$ element of the matrix E and not to $E_i(j)$. The constant multipliers, c_i, can be obtained as

$$\left\{ \begin{array}{c} c_1(\omega) \\ c_2(\omega) \\ c_3(\omega) \end{array} \right\} = -\frac{1}{i\omega} (AB)^{-1} \left\{ \begin{array}{c} \hat{p}(\omega) \\ \hat{q}(\omega) \\ 0 \end{array} \right\} \tag{3.61}$$

$$A = \begin{bmatrix} C_{21} & C_{22} & C_{23} & C_{24} & C_{25} & C_{26} \\ C_{61} & C_{62} & C_{63} & C_{64} & C_{65} & C_{66} \\ C_{41} & C_{42} & C_{43} & C_{44} & C_{45} & C_{46} \end{bmatrix} \tag{3.62}$$

where $\hat{p}(\omega)$ and $\hat{q}(\omega)$ are the Fourier transforms of the contact pressure and the shear traction respectively. Numerical implementation of the above method is done using the Fast Fourier Transform (FFT) method.

4. Friction Coefficient

4.1 Introduction

Wear of pads and specimens causes the coefficient of friction to increase during the fretting fatigue process. Many of the load-controlled fretting experiments are conducted in the regime of mixed-mode fretting (Farris et al. 2003). Due to low coefficient of friction in the beginning of the experiment, the applied tangential load causes sliding of the two contacting surfaces ($Q = \mu_o P$). After sometime, the coefficient of friction increases leading to partial slip. The transition from sliding to partial slip is borne out by full-field infrared measurements of temperature (Harish et al. 2000). This transition from sliding to partial slip is called mixed-mode fretting. Careful experiments are required to characterize the coefficient of friction in the slip zones. Measurement of friction coefficient in this slip zone is required for accurate evaluation of contact stresses.

4.2 Procedure for Friction Coefficient Evaluation Tests

Friction experiments aimed at characterizing the evolution of the coefficient of friction in the slip zones, μ_s, with number of cycles in a partial slip experiment were conducted. As the coefficient of friction increases with the fretting damage, the tangential force stabilizes at a value less than that required for gross sliding. Thus, the coefficient of friction cannot be evaluated as the magnitude of tangential force divided by the normal force. Hence, an alternative approach, that requires a special load history, was taken to evaluate the slip zone coefficient of friction.

After running the fretting test for a specified number of fretting cycles at which we want to determine the friction coefficient, the test was stopped. The average

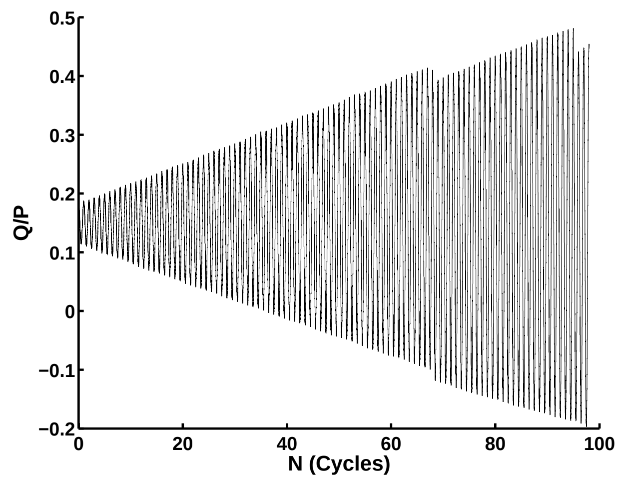

Figure 4.1. Increasing amplitude waveform applied to determine the average coefficient of friction. This waveform is applied after running a fretting test for a fixed number of cycles.

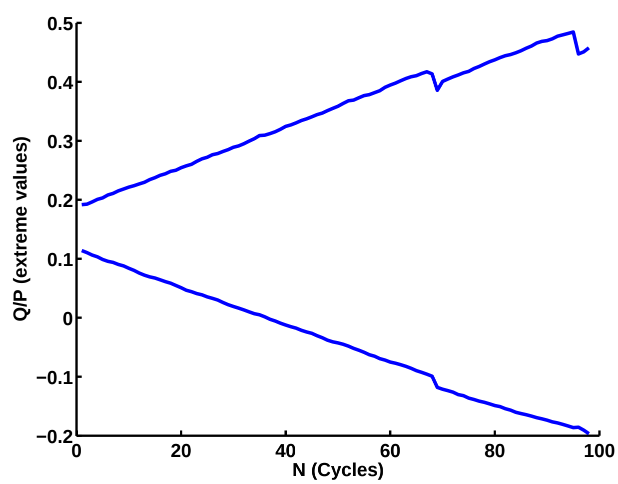

Figure 4.2. Extreme values of Q/P during the application of increasing amplitude waveform.

Table 4.1. Experimental conditions for fretting tests run before applying increasing amplitude waveform and the average friction coefficient obtained after applying the waveform. Cylindrical pads of radius 178mm were used in these tests.

Expt. No.	P (kN/m)	Q_{max} (kN/m)	Q_{min} (kN/m)	σ_{max} (MPa)	σ_{min} (MPa)	N (Cycles)	μ_{av}	Q_{max}/P	μ_s
1	2662	N/A	N/A	N/A	N/A	0	0.48	N/A	0.48
2	2609	877	-75	309.6	0.0	600	0.49	0.336	0.51
3	2541	899	-82	309.6	0.0	2500	0.56	0.354	0.65
4	2713	962	-42	312.6	6.7	10000	0.56	0.355	0.65

coefficient of friction was now determined in the following way. Without disturbing the pad/specimen contact, an increasing amplitude waveform is applied to the specimen. This causes the tangential force to increase during each "friction cycle". Figure 4.1 shows the Q/P evolution during one such friction test. Ultimately, the tangential force reaches the value required for gross sliding, and the experiment is stopped. When the tangential force reaches the value required for gross sliding and the pad starts sliding, the value of Q/P drops slightly as can be observed in figure 4.1(a). This drop can be better demonstrated by plotting only the extreme values of Q/P values experienced during the test (Figure 4.2). In the laboratory, the sliding of pad against specimen also results in a sharp sound, from which we can determine the time when the sliding has occurred and hence stop the test. The ramping parameters are chosen such that the number of friction cycles required is about 100. The maximum value of the tangential force before sliding commences divided by the normal force gives the average coefficient of friction.

Two different sets of pads were used to obtain the friction coefficient. One set of pads were machined to have a cylindrical profile of radius 178 mm. Other set of pads were nominally flat with a flat length of 3.05 mm with 3.05 mm radii at the edges. The average friction coefficients obtained using the two different profiles are listed in Tables 4.1 & 4.2 along with the load conditions under which the fretting tests were run, before the increasing amplitude waveform was applied. In some of

Table 4.2. Experimental conditions for fretting tests run before applying increasing amplitude waveform and the average friction coefficient obtained after applying the waveform. Nominally flat pads of flat length 3.05mm and edge radii of 3.05mm were used in these tests.

Expt. No.	P (kN/m)	Q_{max} (kN/m)	Q_{min} (kN/m)	σ_{max} (MPa)	σ_{min} (MPa)	N (Cycles)	μ_{av}	Q_{max}/P	μ_s
5	2611	N/A	N/A	N/A	N/A	0	0.42	N/A	0.42
6	2507	672	-322	314.1	7.7	20000	0.44	0.268	0.5
16	3404	N/A	N/A	N/A	N/A	0	0.41	N/A	0.42
17	3346	813	-9	278.2	11.0	1000	0.43	0.243	0.48
18	3351	871	40	286.5	16.9	10000	0.44	0.260	0.5
7	2793	N/A	N/A	N/A	N/A	0	0.42	N/A	0.42
8	2763	1004	58	314.1	9.2	2000	0.41	0.363	0.41
9	2763	985	40	317.8	12.9	10000	0.45	0.357	0.53
10	2683	N/A	N/A	N/A	N/A	0	0.42	N/A	0.42
11	2654	934	-467	312.6	6.1	2000	0.5	0.352	0.58
12	2639	992	13	315.0	5.7	10000	0.48	0.376	0.56
13	2572	N/A	N/A	N/A	N/A	0	0.5	N/A	0.42
14	2524	969	16	309.5	3.7	1000	0.42	0.384	0.42
15	2531	911	-35	308.0	3.1	5000	0.57	0.360	0.63
19	2545	N/A	N/A	N/A	N/A	0	0.52	N/A	0.52
20	2517	941	-37	310.4	-1.8	1000	0.58	0.374	0.64
21	2531	901	-107	310.1	0.0	5000	0.59	0.356	0.65

the tests, friction was determined at 0 cycles implying that no fretting test was run before applying the increasing amplitude waveform. Therefore there are no loading conditions reported for those tests.

Following observations could be made from the friction tests:

(a) Average friction coefficient was observed to be higher in case of cylindrical pads as compared with nominally flat pads.

(b) Average friction coefficient was observed to be higher in case of nominally flat pads when subjected to higher Q/P ratios and higher bulk stress.

One of the implications of the above set of observations might be that the average friction coefficient increases if the slip zone size is larger and/or magnitude of slip is larger. The slip zone size is typically larger in cylindrical pads as compared with the nominally flat pads. The slip zone also increases with increase in Q/P ratio.

4.3 Evaluation of Slip Zone Friction Coefficient

When the pad and the specimen are made from similar isotropic materials an approach outlined by Hills & Nowell (1994) is used to determine the slip zone coefficient of friction, μ_s, in terms of the average coefficient of friction, μ, and the initial coefficient of friction, μ_0 (Murthy et al. 2000). This formulation (Hills & Nowell 1994) is only suitable when the pressures distribution is given by the Hertzian pressure distribution. In the case of contact of dissimilar isotropic/anisotropic materials the pressure is not only not Hertzian but also the solutions for the contact pressure and the shear traction are coupled. Hence, a closed form relation between μ_s, μ, and μ_0 cannot be simply deduced.

A new numerical method has been devised to obtain μ_s in terms of μ, and μ_0 for the case of dissimilar isotropic materials. Essentially μ_s is increased in an incremental manner, starting from μ_0, until the solution of the sliding contact problem yields the experimentally measured average coefficient of friction, μ. As with the Hills & Nowell approach we assume that μ_s is constant in the slip zones, and the coefficient of friction in the stick zones does not change Initially the coefficient of friction is assumed to be constant ($= \mu_0$) through out the contact zone. As the slip zone coefficient of friction increases so does the stick zone size. In each increment the ends of the stick zone are determined by solving the partial slip contact problem taking into account the remote tension applied on the specimen and the material dissimilarity of the pad and the specimen. Keeping track of the previous increments allows us to determine the distribution of the coefficient of friction within the contact zone in the current increment, $\mu_i(x)$. Hence, the sliding contact problem for a given increment can be written as,

$$\frac{\partial H}{\partial x} + C_1 = k_1 \mu_i(x) q(x) - \frac{k_2}{\pi} \int_{a_1}^{a_2} \frac{p(t)}{t-x} dt \tag{4.1}$$

where $H(x)$ is the gap function, $p(x)$ and $q(x)$ are the pressure and the shear traction respectively, a_1 and a_2 are the ends of the contact zone and the constants k_1 and k_2 are obtained from the elastic material properties of the two contacting bodies (described in the next section). Once the sliding contact problem is solved the average coefficient of friction in a given increment is obtained as,

$$\mu = \frac{\int_{a_1}^{a_2} \mu_i(x) p(x)\, dx}{\int_{a_1}^{a_2} p(x)\, dx} \tag{4.2}$$

where a_1 and a_2 are the ends of the contact zone.A

The slip zone coefficients evaluated by the above procedure for the friction tests conducted using the setup are presented in Tables 4.1 & 4.2. As can be seen, both from average friction coefficient and slip zone friction coefficient, there is a dependence of friction coefficient on Q/P ratio. While using friction coefficient in the analysis of experiments, this dependence of friction coefficient on Q/P ratio was taken into consideration by assuming a linear variation of friction coefficient with Q/P ratio.

5. Experimental Observations

5.1 Fractography

The analysis and characterization of the fretting fatigue fracture surfaces is essential to develop an inherent understanding and description of fretting fatigue fractographic features associated with single crystal nickel at high temperatures. Preliminary observations of the fracture surface have been presented. A fracture surface of a SCN dog-bone specimen can be seen in Figure 5.1. The fracture surface is highly crystallographic in a macroscopic view. The fracture plane was determined with respect to the specimen coordinate system using a *Co-ordinate Measuring Machine* (CMM). Two mutually perpendicular fracture surfaces were observed in case of specimens with secondary orientations close to 45^o to the contact surface. Figure 5.2 shows the schematic of the angles measured by the CMM. θ_1 is the angle between the normal, OA, and the axis of the specimen. θ_2 is the angle between the projection of the normal in YZ plane, OB, and the y-axis. The angles measured from the CMM have been reported in Table 5.1. Comparing the angles measured by the CMM with the material principal axes obtained from Lauè diffraction, it was observed that the

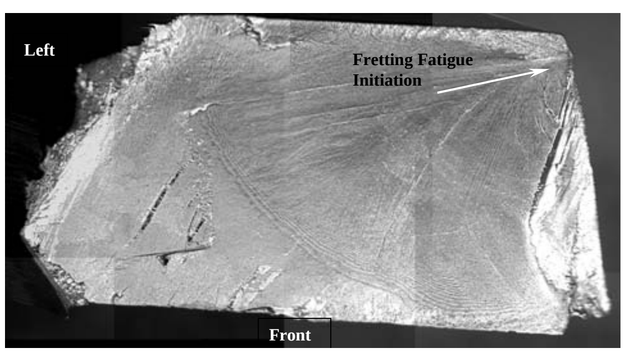

Figure 5.1. Fretting fatigue fracture surface 10X. Specimen ZOKKA.

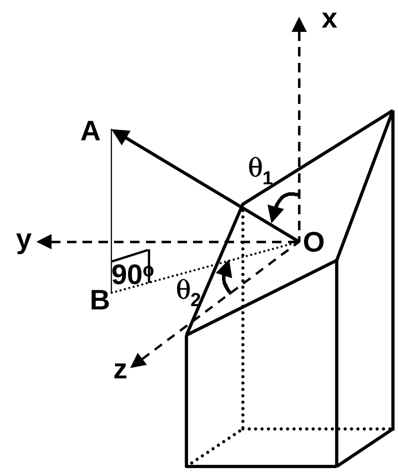

Figure 5.2. Schematic of the angles measured by the CMM. θ_1 is the angle between the normal, OA, and the axis of the specimen. θ_2 is the angle between the projection of the normal in YZ plane, OB, and the y-axis.

fracture plane was along $\{1\ 1\ 1\}$ within a few degrees. The fracture observed along the <111> macro-plane is similar to findings of other researchers (Cunningham et al. 1996) .

The initiation region is indicated in the Figure 5.1, and it was also verified to have initiated at the edge of contact of the contact pad and dog-bone specimen. The region of initiation is shown in Figure 5.3. It can be seen that the crystallographic region transitions into a flat region, which was found to be perpendicular to the contact region. A closer view of the flat region is also presented in Figure 5.3.The flat region appears to have been compacted as expected in fretting fatigue of isotropic materials. The transition region from the fretting crack to the macroscopic crystallographic fracture showed some evidence of being mono-planar trans-precipitate non-crystallographic (TPNC), but more work is necessary to verify these findings.

5.2 Determination of Material Principal Axes

Orientation of the primary axis of the material with respect to axis of the specimen was obtained from the manufacturer. However, since the orientation of secondary

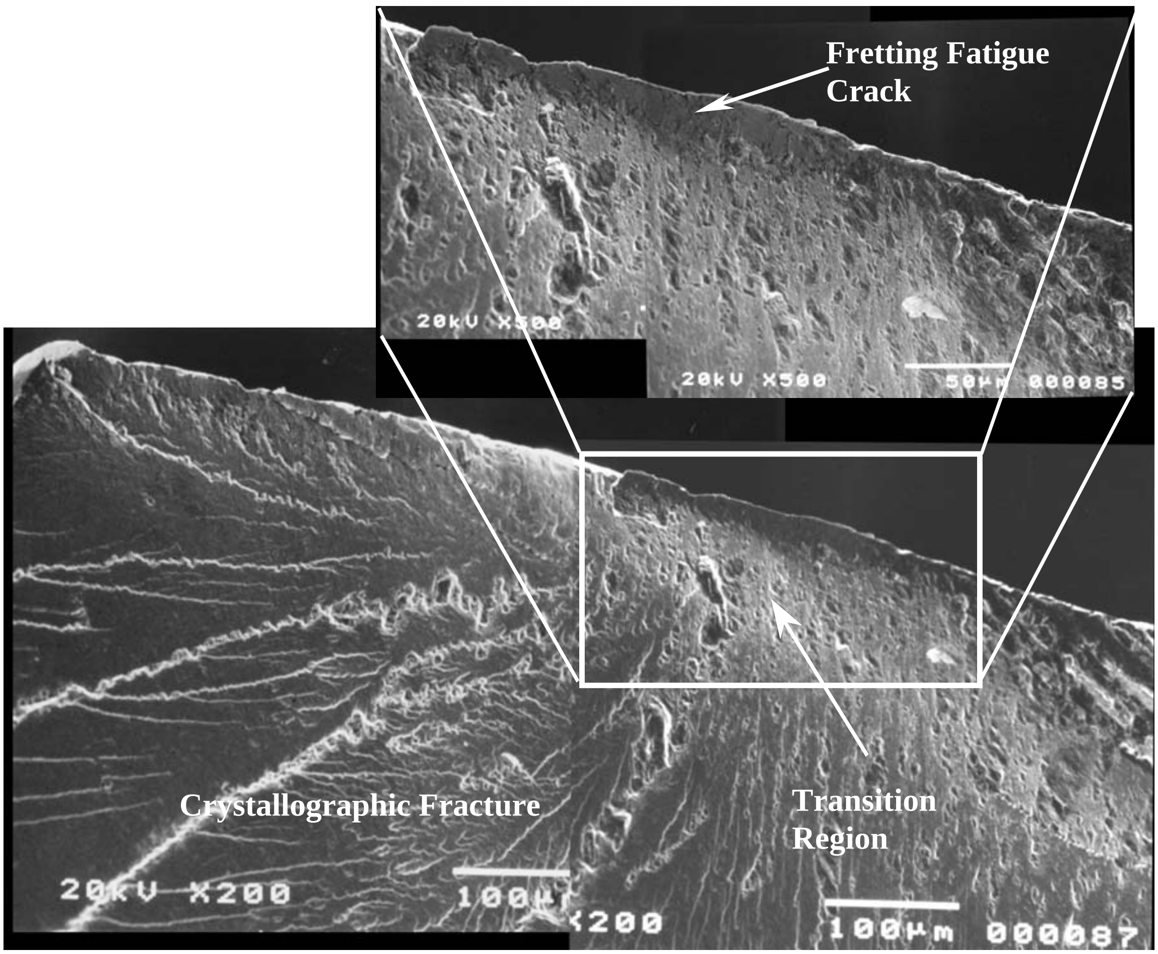

Figure 5.3. SEM fractographs of fretting fatigue crack in ZOKKA specimen.

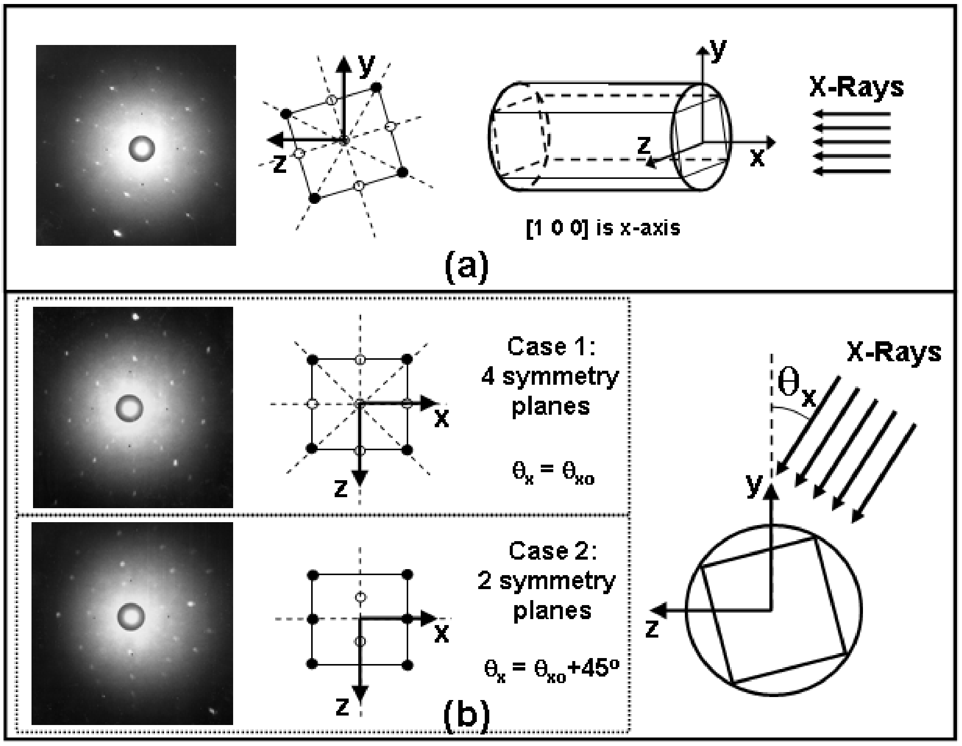

Figure 5.4. (a) Lauè diffraction as produced by orienting x-rays along primary axis of specimen. (b) Schematic highlighting procedure of identifying secondary and tertiary material axis orientations. Note that the dotted lines represent planes of symmetry in the FCC construction of SCN.

axis with respect to the contacting surface was not known, SIE analysis (detailed in subsequent sections) was performed for all possible orientations. As can be seen from Figure 2.7(b) the effect of orientation of the secondary axes on subsurface stresses is significant. A Lauè x-ray diffraction method was used to determine the orientation of the material principal axes to facilitate an accurate stress analysis. The process is shown schematically in Figure 5.4. Since the direction <1 0 0> is very close to the axis of the specimen, Lauè diffraction pattern of the specimen was taken by projecting the beam along the axis of the specimen. A typical diffraction pattern obtained from the Lauè setup is illustrated in Figure 5.5. Since the material has a Face Centered Cubic (FCC) structure, when we look along <1 0 0> direction, the pattern has four symmetry planes as can be observed in Figure 5.5. One set of symmetry planes

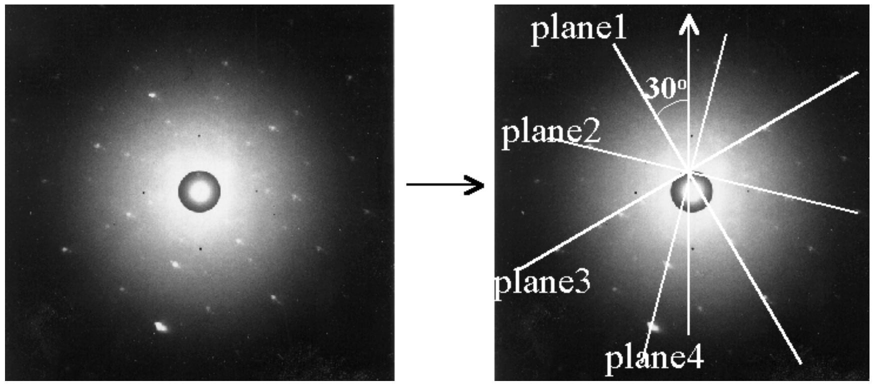

Figure 5.5. Laue Pattern of specimen $ZOKKA$ along <1 0 0> direction (specimen axis). Four planes of symmetry can be observed.

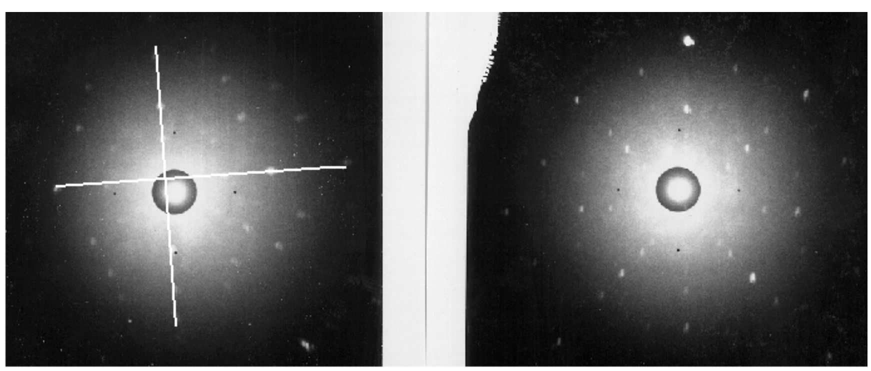

Figure 5.6. (a) Laue pattern of $ZOKKA$ along <0 1 1>. Only two planes of symmetry are visible. (b) Laue pattern of $ZOKKA$ along <0 1 0>. Four planes of symmetry are visible.

correspond to the {0 1 0} and {0 0 1} planes, while the other set corresponds to {0 1 1} and {0 1 -1} planes. In order to determine which set of mutually perpendicular planes corresponds to the {0 1 0} and {0 0 1} planes, the surface perpendicular to the specimen axis was polished and used for obtaining Lauè pattern. The beam was then projected along one of the symmetry planes and then along the other symmetry plane at 45^o to the first plane. When the beam is projected along the <0 1 0> or <0 0 1> directions, the pattern will match the observed pattern along the <1 0 0> direction(Figure 5.6(b)). When the beam is along <0 1 1> or <0 1 -1> direction, only one set of symmetry planes are observed in the pattern (Figure 5.6(a)). Thus, knowing the primary orientation <1 0 0> (provided by the vendors), and from Lauè diffraction patterns, the secondary axis <0 1 0> and the teritiary axis <0 0 1> were determined and are as listed in the Table 5.1. For the specimens which did not fail, secondary axis could not be determined since the specimen could not be sectioned for the purpose.

Table 5.1. Angles obtained from Lauè patterns and the CMM. All angles are in degrees. Please refer to Figures 5.4 and 5.2 for the details of the angles.

Expt. No.	Specimen	Lauè Pattern		Angles from CMM			
		Primary axis	Secondary axis	Plane 1		Plane 2	
		θ_z	θ_x	θ_1	θ_2	θ_1	θ_2
2	ZOKLE	3	15	52	28		
4	ZOKJW	6	-14	50	58		
5	ZOKKE	2.5	45	54	90	51	2
6	ZOKKD	2	-40	56	85	56	-7
7	ZOKKA	3	-15	57	60.5		
8	ZOKFR	1	23	52	24		
9	ZOKJJ	3	33	58	80		
10	ZOKMI	2	43	53.5	2		
11	ZOKG9	1	44	56.5	3		
12	ZOKHX	0	-8	56	54		
13	ZOKLU	1	2	56	44	56	45
14	ZOKH9	1	-22	57	66		
15	ZOKFM	0	-6.4	55	87	59	6
16	ZOKHA	2.5	23	53	20		
17	ZOKLK	1	-13.5	56	60		
19	ZOKDK	2	28	53	19		
20	ZOKFL	0	-20	56	62		
23	ZOKGD	3	17	54	30		
24	ZOKGS	2	-38	53	-9	53	82
26	ZOKFP	3	-14	54	58		

6. Life Estimation

6.1 Lifing Approaches

Current research has led to the development of several fretting fatigue analysis and modelling schemes. These analysis schemes fall generally into three categories: (1) fracture mechanics approaches, (2) a new crack analogue approach investigating equivalences between contact mechanics and fracture mechanics, and (3) stress based approaches. In each of these cases, it is very essential to know the highly localized multi-axial stress field resulting from oscillatory shear and normal loads in fretting contact, an accurate understanding of the near contact stresses as well as the sub-surface bulk stress. These contact stresses can be obtained from Green's functions as discussed earlier in the report or by finite element stress analysis.

6.1.1 Fracture Mechanics Approaches

Since fretting fatigue cracks have been found to be initiated very early during life of the specimen (Endo 1981), several researchers have investigated the application of fracture mechanics in analyzing the fretting problem. The crack tip stress intensity factors for the calculated stress field can be obtained from distributed dislocation methods (Hills & Nowell 1994). Once the crack grows beyond the influence of the contact forces, the subsurface bulk stresses dominate and familiar fatigue crack growth models can be implemented. A subsequent fretting fatigue life prediction can then be maintained by integrating a fretting fatigue crack growth law. This method was shown to have some success in predicting experimentally derived S-N curves (Edwards 1981). Other work has compared the composite ΔK_{app} arising in fretting problems with an experimentally determined threshold stress intensity factor, ΔK_{th}, in efforts to identify a balance between crack growth and arrest (Lindley 1997, Hattori et al. 1988). It has been shown that the stress intensity factor for a small crack, ΔK_{app} increases for conditions of fretting fatigue. This can lead to sustained crack propagation if $\Delta K_{app} > \Delta K_{th}$ and suggests that fretting could foster fatigue crack growth when arrest would have occurred without the contact stresses present.

6.1.2 Crack Analogue Approach

A recent fretting fatigue analysis method developed by Giannakopoulos et al. (1998) involves identifying certain aspects of equivalence between contact mechanics and fracture mechanics. This *crack analogue* model involves drawing an analogy between the near tip crack geometry seen in specimens and the sharp edged geometry observed at the edge of contact for two contacting bodies. For a given set of elastic properties, contact mechanics can be used to show a square root stress singularity behavior at the edge of contact. This asymptotic stress behavior as seen in the stress and strain fields at the edge of contact can be shown to be equivalent to the stress behavior seen in the vicinity of the crack tip in linear elastic fracture mechanics for similar geometries. The contact punch and substrate combination leads to the definition of a fictitious crack length which allows a physical basis for initiation and propagation analyses. Further efforts have been performed to investigate the effect of roundness on a nominally sharp contact geometry by developing a *notch analogue* approach (Giannakopoulos et al. 2000).

6.1.3 Stress Based Approaches

There has been some success in predicting the fretting fatigue life using mechanics or stress based models. Conventionally, stress based approaches have involved the acquisition of S-N curves with and without the fretting contact. The resulting data then provides a basis for determining a corresponding fretting fatigue strength reduction factor. This method allows the ranking of variables (or combination of variables) as to their contribution to overall fretting fatigue performance. Mechanics based models are formulated from information about the contact pressure, external load (or bulk load), coefficient of friction, and tangential load (or relative slip). The fact that these models show success for a variety of testing conditions suggests that all other *secondary* effects could collapse into or be a part of the effects of the previous four *primary* variables (Dobromirski 1992). Due to these successes and the development of a quasi-analytical approach to obtain contact stresses (Rajeev & Farris 2002), stress based approaches were investigated in course of the current research efforts.

6.2 Stress Based Approach for Predicting Nucleation

A few research efforts have attempted to correlate a mechanics-based understanding of partial slip contacts and fretting crack nucleation (Petiot et al. 1995, Fellows et al. 1997). Others have suggested the use of fretting fatigue parameters comprising products of interfacial shear, tangential stress and slip amplitude (Ruiz et al. 1984). Szolwinski and Farris have offered (Szolwinski & Farris 1996) and validated (Szolwinski & Farris 1998) an approach for predicting fretting crack nucleation through application of a multi-axial fatigue life parameter, Γ, proposed by Smith, Watson and Topper (Bannantine et al. 1990) that links the near-surface cyclic stresses and strains to the number of cycles required to nucleate a crack along a critical plane in Al2024-T3 material. Murthy et al. (2001) have used an equivalent stress parameter, σ_{eq}, obtained from the surface stresses, to quantify crack nucleation in Ti-6Al-4V. Inspired by the correlation obtained by using these multi-axial parameters in fretting fatigue of isotropic materials, an attempt was made to investigate different multi-axial parameters for anisotropic contacts. The stress based approach assumes that once the proper contact stresses are obtained by a robust tool, the problem of fretting crack nucleation can be treated as a fatigue problem with stress concentration. Therefore, coventional parameters used for fatigue crack nucleation parameters can be used to predict fretting crack nucleation using the contact stresses.

6.2.1 Prediction of Uniaxial Fatigue Tests

The first step in the investigation of nucleation parameters involves verifying the validity of parameters in predicting the nucleation lives in uniaxial fatigue tests. In order to achieve this, uniaxial fatigue tests conducted with the material identical to the one used in fretting fatigue experiments were analyzed. The uniaxial tests were run by laboratories at General Electric Aircraft Engines (GEAE) and Pratt & Whitney Engines (PWE). Arakere & Swanson (2001) have studied applicability of some of the multi-axial parameters to uniaxial fatigue tests conducted with a similar single crystal nickel superalloy. Naik et. al. have studied similar set of parameters for application to uniaxial fatigue tests conducted with same material as is used in the current study. Data obtained from uniaxial tests conducted by PWE and GEAE were studied with the following parameters:

1. Maximum shear stress range (SSR) along the critical plane.

2. Socie's parameter defined as (Socie 1987)
   $SOC = \frac{\Delta\gamma}{2} + \frac{\Delta\epsilon_n}{2} + \frac{\sigma_{no}}{2E}$
   where $\frac{\Delta\gamma}{2}$ is the amplitude of shear strain, $\frac{\Delta\epsilon_n}{2}$ is the amplitude of the normal strain, and σ_{no} is the maximum normal stress.

3. Findley's (Findley 1959) parameter defined as $FIN = \tau_a + k\sigma_{max}$, where τ_a is the amplitude of the shear and σ_{max} is the maximum value of stress normal to the plane along which shear is occurring.

4. Fatemi-Socie-Kurath (Fatemi & Socie 1988) parameter defined as $FSK = \gamma_a\,(1 + \frac{k\sigma_n^{max}}{\sigma_y}$, where γ_a is the shear strain amplitude on a critical slip direction, σ_n^{max} is the maximum value of stress normal to the plane along which shear is occurring, and σ_y is the yield stress.

5. Chu-Conle-Bonnen parameter defined as:
   $CCB = 2\gamma_a\tau_{max} + \epsilon_a\sigma_{max}$
   where γ_a is the shear strain amplitude, τ_{max} is the maximum shear stress, ϵ_a is

the normal strain amplitude, and σmax is the maximum normal stress. CCB parameter is a work based criterion developed by Chu et al. (1993). It is a combined shear and normal criterion that uses Smith-Watson-Topper type of work form instead of using strain amplitude as the parameter form.

6. McDiarmid parameter defined as:

   $McD = \tau_a + k\sigma_{max}$, where τ_a is the amplitude of the shear and σ_{max} is the maximum value of stress normal to the plane along which shear is occurring. It is similar to the Findley parameter. Crucial difference being the way critical plane is defined. In Findley parameter, as with the other parameters discussed in this section, critical plane is the plane along which the parameter is maximum. In McDiarmid parameter, critical plane is the plane along which τ_a is maximum.

7. Smith-Watson-Topper (Bannantine et al. 1990) parameter defined as:

   $\Gamma = \epsilon_a \sigma_{max}$

   where ϵ_a is the normal strain amplitude, and σ_{max} is the maximum normal stress.

8. The parameter σ_{eq} is defined as (Doner et al. 1982),

$$\sigma_{eq} = 0.5(\Delta\sigma_{psu})^w(\sigma_{max})^{(1-w)} \ . \tag{6.1}$$

The stress invariant effective stress range is defined as,

$$\begin{aligned}\Delta\sigma_{psu} = & \frac{1}{\sqrt{2}}\Big[(\Delta\sigma_{xx} - \Delta\sigma_{yy})^2 + (\Delta\sigma_{yy} - \Delta\sigma_{zz})^2 \\ & +(\Delta\sigma_{zz} - \Delta\sigma_{xx})^2 + 6(\Delta\sigma_{xy}^2 + \Delta\sigma_{yz}^2 + \Delta\sigma_{zx}^2)\Big]^{\frac{1}{2}} \ ,\end{aligned} \tag{6.2}$$

where $\Delta\sigma_{psu}$ is the alternating pseudo-stress range, and $\Delta\sigma_{ij}$ defines the pseudo-stress range for each stress component based on maximum and minimum points in the fatigue cycle. The Manson-McKnight mean stress term used to establish σ_{mean} and σ_{max} is given as,

$$\begin{aligned}\Delta\sigma_{mean} = & \frac{\beta}{2\sqrt{2}}\Big[(\Sigma\sigma_{xx} - \Sigma\sigma_{yy})^2 + (\Sigma\sigma_{yy} - \Sigma\sigma_{zz})^2 \\ & +(\Sigma\sigma_{zz} - \Sigma\sigma_{xx})^2 + 6(\Sigma\sigma_{xy}^2 + \Sigma\sigma_{yz}^2 + \Sigma\sigma_{zx}^2)\Big]^{\frac{1}{2}} \ ,\end{aligned} \tag{6.3}$$

Table 6.1. Curve fit values for different nucleation parameters. The curve fit was assumed to be of the form $Damageparameter = A(N)^{-b}$

Damage Parameter	A	b	Correlation factor (R^2)
SSR (MPa)	332.5	0.0573	0.2267
SOC	0.0127	0.0598	0.6238
FIN (MPa)	1449	0.0861	0.5781
FSK	0.0118	0.0622	0.313
CCB (MPa)	9.851	0.1007	0.6931
McD (MPa)	723.3	0.0569	0.2752
Γ (MPa)	3.160	0.2685	0.5128
σ_{eq} (MPa)	638.6	0.0403	0.6579

where σ_{mean} is the mean stress, and $\Sigma\sigma_{ij}$ represents the summed stress for each stress component based on maximum and minimum points in the fatigue cycle. The Manson-McKnight coefficient ($\beta = \beta_{MM}$) is defined as:

$$\beta_{MM} = \frac{\Sigma\sigma_1 + \Sigma\sigma_3}{\Sigma\sigma_1 - \Sigma\sigma_3}\ , \tag{6.4}$$

where $\Sigma\sigma_1$ is the sum of the first principle stresses at the maximum and minimum stress points in the fatigue cycle and $\Sigma\sigma_3$ is the sum of the third principle stress at the maximum and minimum stress points in the fatigue cycle.

Figures 6.1 and 6.2 show the results of analysis of uniaxial fatigue tests. They also include curve fits of the form $Damage\ parameter = A(N)^{-b}$. Table 6.1 lists the curve fit parameters A, b, and correlation factor R^2 for each of the nucleation parameters.

Four of the parameters, SOC, FIN, CCB and σ_{eq}, with highest correlation factors for uniaxial fatigue tests were used for analysis of fretting tests.

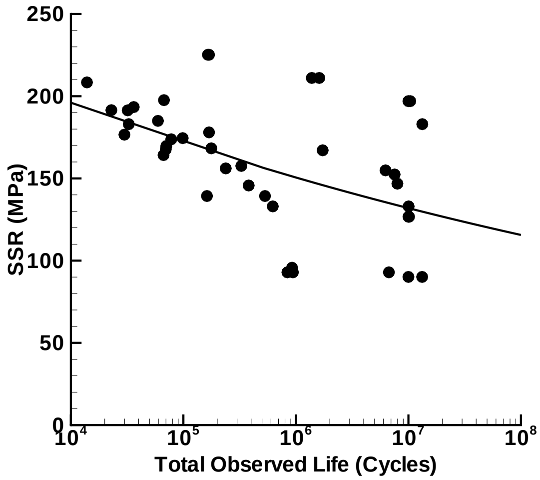

(a) SSR parameter.

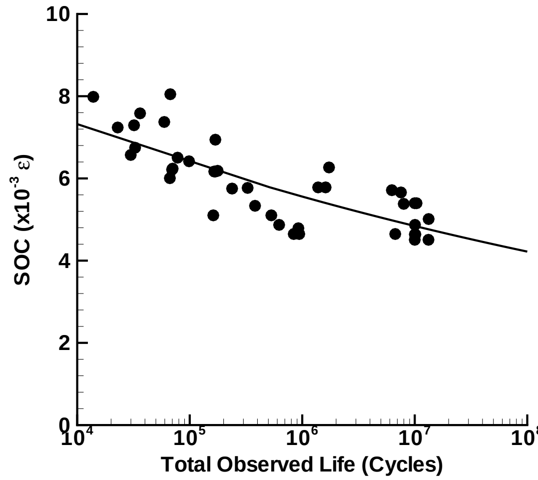

(b) Socie's parameter.

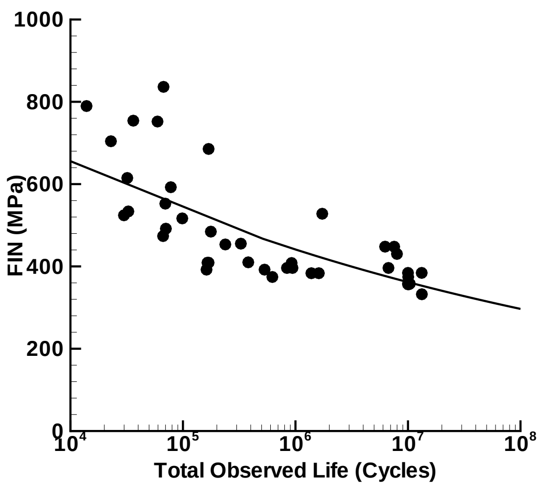

(c) Findley parameter.

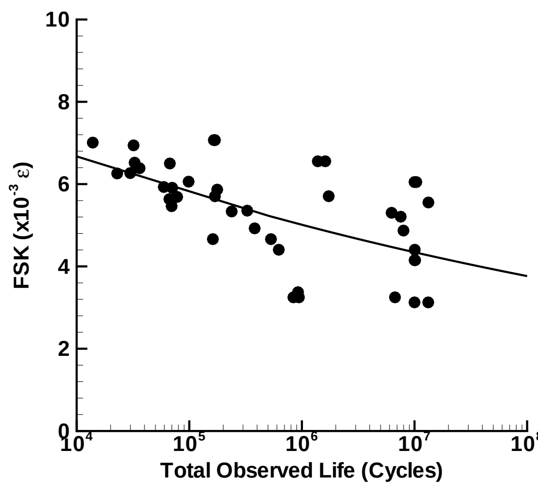

(d) FSK parameter.

Figure 6.1. Comparison of uniaxial data and fretting data with different lifing parameters.

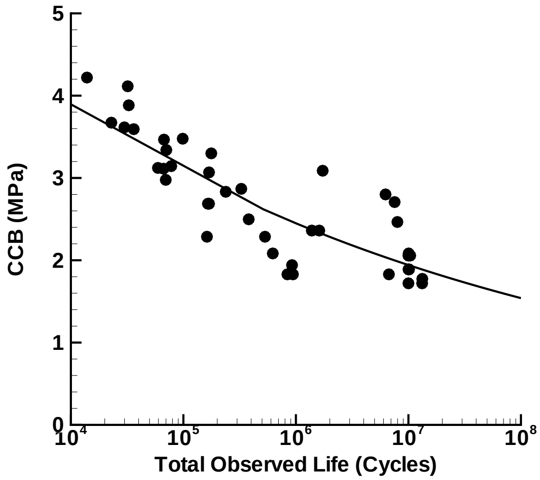

(a) CCB parameter.

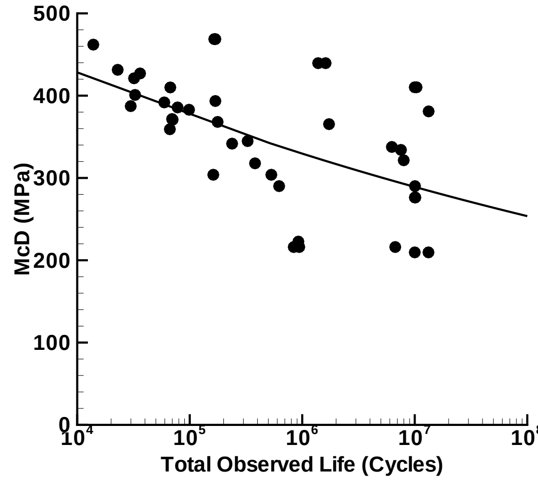

(b) McD parameter.

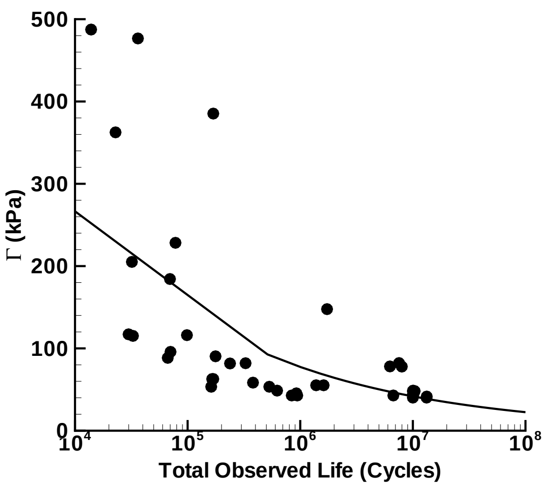

(c) Γ parameter.

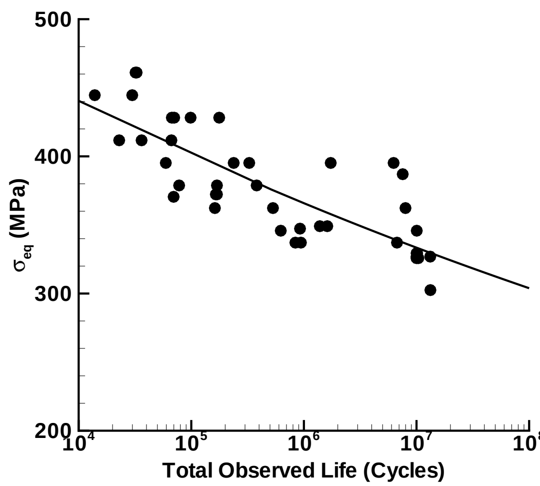

(d) σ_{eq} parameter.

Figure 6.2. Comparison of uniaxial data and fretting data with different lifing parameters.

6.3 Stressed Area Correction

Experiments with Ti-6Al-4V suggested that higher peak stresses are required to produce failure in notched specimens as compared to smooth specimens using the same σ_{eq} life metric. The predictive capability improved when σ_{eq} was averaged over few elements near the surface and the averaged value was used as the damage metric. Still this approach did not significantly improve the correlation for the notched specimens, since the calculated σ_{eq} was substantially higher as compared to all other geometries with similar life (Murthy et al. 2001) . Due to these difficulties a weak link approach (Batdorf & Heinisch 1978) was considered to evaluate the fatigue crack initiation life for stress concentrations. This approach recognizes that it is less likely for a weak grain to exist at the surface of a small notch as compared to the probability of finding a weak grain on the surface of a very large notch or a smooth specimen. The weak link approach predicted the results very well for notched specimens (Murthy et al. 2001). Weakest link approaches are routinely applied to monolithic ceramics and high strength composite fibers (Schenk et al. 2000). A stressed surface area was evaluated as compared to volume since nearly all of the initiation sites appeared to be on or very near the surface of the specimens. In addition, the stress gradient on the surface is also representative of the stress gradient along the depth in isotropic materials.

In the weakest link approach, the probability of survival, R, of a small area, ΔA_i, subjected to a damage parameter of ϕ_i is assumed to be:

$$(R_o(\phi_i))^{\Delta A_i} = (exp[-(\frac{\phi_i}{\beta})^\alpha])^{\Delta A_i} \ . \tag{6.5}$$

The above formulation assumes a two parameter Weibull distribution with α as the shape factor and β as the scale parameter. The probability of survival of all the stressed areas would then be given by:

$$\ln(R) = \sum_{i=1}^{n}[\ln R_o(\phi_i)]\Delta A_i \ . \tag{6.6}$$

If two specimens have same life, then their probability of survival is the same. By equating the two probabilities, we get,

$$(\frac{\phi_{max,1}}{\beta})^{\alpha} Fs_1 = (\frac{\phi_{max,2}}{\beta})^{\alpha} Fs_2 \ , \tag{6.7}$$

where parameter Fs is given by,

$$Fs_j = \sum_{i=1}^{n} [-(\frac{\phi_{i,j}}{\phi_{max,j}})^{\alpha}] \Delta A_{i,j} \ , \tag{6.8}$$

Hence we get an equivalent damage parameter corresponding the smooth bar data as,

$$\phi_{eq} = (\frac{Fs_2}{Fs_1})^{\frac{1}{\alpha}} \phi_{max} \ , \tag{6.9}$$

where ϕ_{max} is the maximum value of damage parameter obtained for the actual experiment and ϕ_{eq} is the equivalent damage parameter in a smooth bar specimen which has the same life as that of the actual experiment. The ϕ_i used is the distribution of damage parameter on the surface. ϕ_{max} is the maximum value of ϕ_i. on the surface. Fs_1, the stressed area for the smooth bar, is the area of the gage section of the smooth bar specimen.

This stressed area approach worked reasonably well for life predictions of notched specimens as well as fretting fatigue specimens made of Ti-6Al-4V (Murthy et al. 2001). A similar stressed area approach was used for the investigations of life estimation parameters with single crystal materials. Any of the lifing parameters discussed in the previous section could be used as the damage parameter ϕ.

6.4 Life Estimation of Laboratory Tests

6.4.1 Stress Analysis

Contact tractions and subsurface stresses were obtained from solution to singular integral equations by a process as detailed in Chapter 3. Prescribed profile of 3.05 mm flat length with 3.05 mm radii at the edges was used to obtain the tractions and the stresses. However, manufacturing tolerances associated with the process of

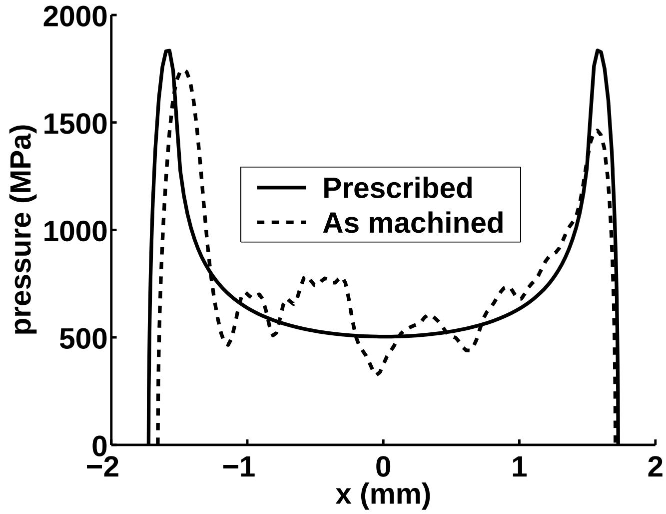

Figure 6.3. Effect of machining tolerances on the surface normal traction. The distance, x, is normalized with respect to the half contact length obtained from the analysis using prescribed profile. Normal force $P = 1.58MN/m$

machining the component alters the profile of the component. Singular integral equation approach is capable of analysing contacts of arbitrary shapes and can be used to study the effect of these manufacturing tolerances on the life estimation. To study the effects of these deviations, an actual profile of a pad machined for a specification of $3.05\,mm$ flat length with $3.05\,mm$ radii at the edges, was compared to the prescribed profile as shown in the Figure 2.8. The pad profile was obtained using a surface profilometer. The profiles were smoothed and analyzed by the singular integral equations approach. Figure 6.3 shows the comparison between the surface normal traction of the two profiles. It can be seen that a small deviation in the profile leads to a significant difference in surface traction leading to a change in sub-surface stress field, hence altering the crack nucleation prediction.

6.4.2 Nucleation paramater evaluation and stress area correction

Uniaxial data obtained from PWE and GEAE were analyzed using different parameters as discussed earlier. Of the different parameters investigated, only four

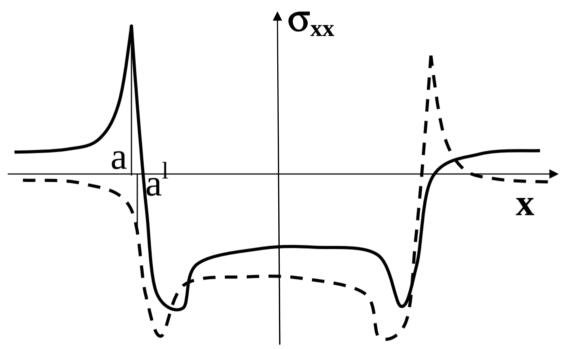

Figure 6.4. A schematic illustration of effect of slip on evaluation of damage parameter.

parameters gave a correlation of about 60% or more. These four parameters were used for nucleation life estimation.

While evaluating the parameters, one of the problems that arise is the fact that the edge of contact where cracks initiate moves in and out of contact because of small amplitude relative slip between pad and specimen at the edge of contact. In other words, the point which experiences the maximum tangential stress when $Q = Q_{max}$, is within the contact region when $Q = Q_{min}$, because of the relative slip between pad and specimen. To account for this relative slip, when evaluating the critical parameter, the value of stress when $Q = Q_{max}$ was taken at $x = a$, where as, it was taken at $x = a'$ when $Q = Q_{min}$ during the cycle as shown in the figure 6.4. a' was chosen such that the difference $a - a'$ corresponds to the slip range at the edge of contact. Since the relative slip is relatively small, effect of this slip on the parameters were typically observed to be relatively less.

The slip also affects the stressed area correction term. Since, the solution the tangential stresses obtained by our analysis are discrete, while evaluating ΔA_i in the equation 6.8, it is assumed to be $\Delta A_i = (\Delta x_i + \Delta slip_i) \times thickness$, at the point where the stress is evaluated (Figure 6.5).

Since the peak stresses were very high, the maximum values of stresses were capped at the yield stress as a first approximation to plasticity effects. Weibull parameter used

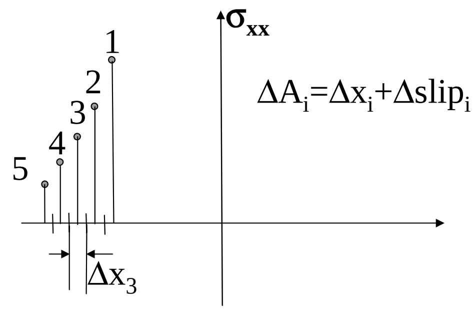

Figure 6.5. A schematic illustration of effect of slip on evaluation of stressed area.

in Ti-6Al-4V was obtained from uniaxial tests conducted with notched specimens. The notches in these specimens acted as stress concentrators. For the material used in fretting fatigue tests, no notched specimen tests could be found in the literature. Therefore $\alpha = 10$ was used since it gave the best correlation factor for fretting tests when compared with the uniaxial curve.

Figures 6.6 - 6.9 show the comparison of uniaxial data with the fretting data using different parameters. CCB parameter and Findley parameter give better predictions than σ_{eq} and Socie parameter. The values of the parameters are listed in Table 6.2. Here the total life is plotted against the damage parameter, which is mainly used for the prediction of nucleation life. In uniaxial tests, the crack nucleation as well as the propagation occurs under same applied stress. Therefore, nucleation life forms the major portion of total life. During fretting fatigue tests, nucleation occurs due to very highly localised contact stresses, whereas the propagation is mostly due to bulk stress which is low relative to the stresses that nucleate the crack. This causes the crack propagation to form a significant portion of total life. Therefore an estimation of crack propagation life is necessary to predict the life of the laboratory specimens.

6.4.3 Estimation of Crack Propagation Lives

The crack that forms is a three-dimensional crack as can be observed from the SEM micrographs of the fracture surface. The cracks initiate on $<1\ 0\ 0>$ plane

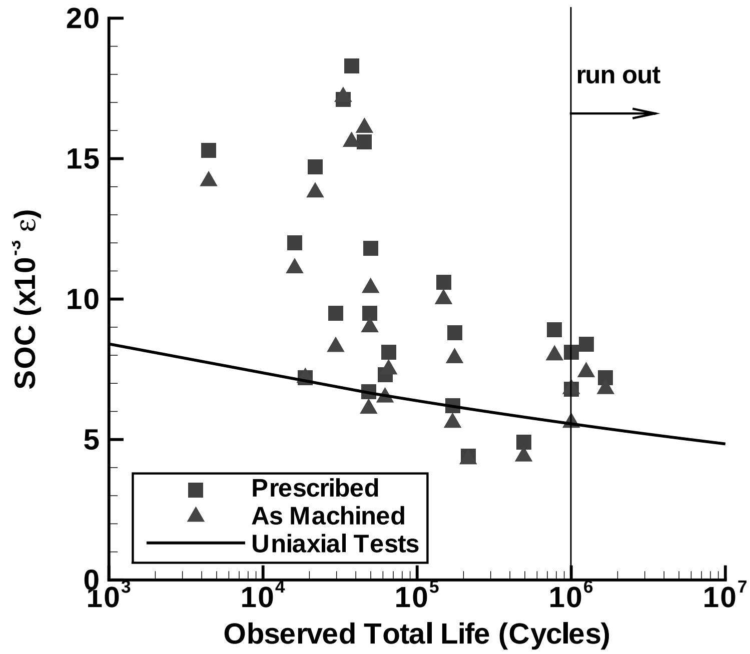

Figure 6.6. Comparison of uniaxial data and fretting data with different lifing parameters - Socie's parameter.

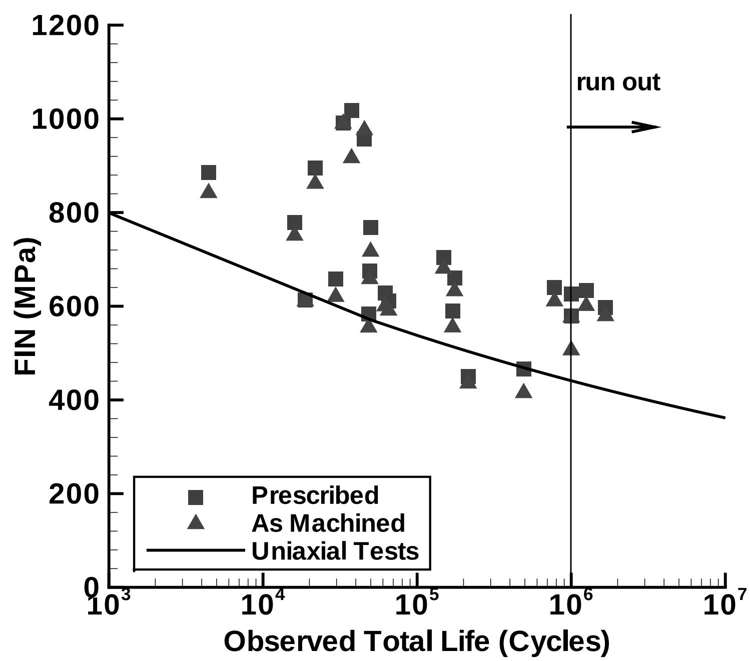

Figure 6.7. Comparison of uniaxial data and fretting data with different lifing parameters - Findley's parameter.

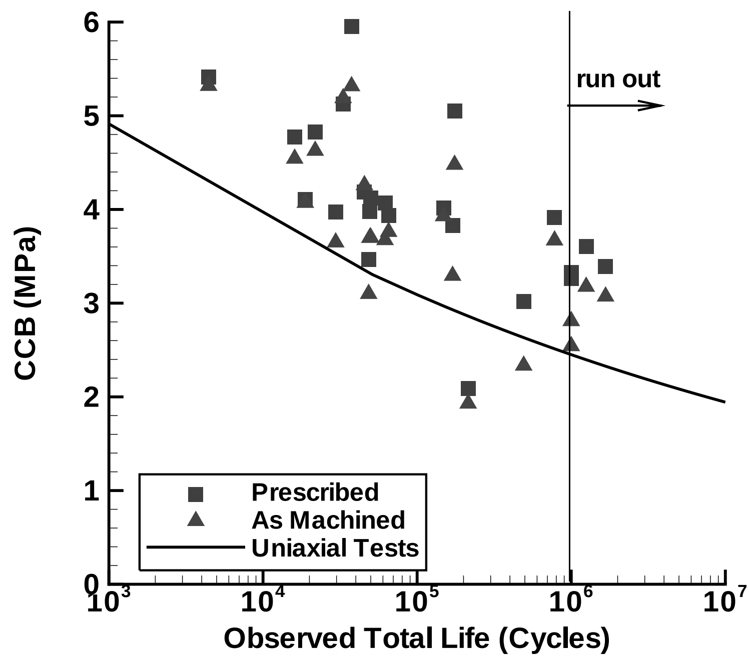

Figure 6.8. Comparison of uniaxial data and fretting data with different lifing parameters - CCB parameter.

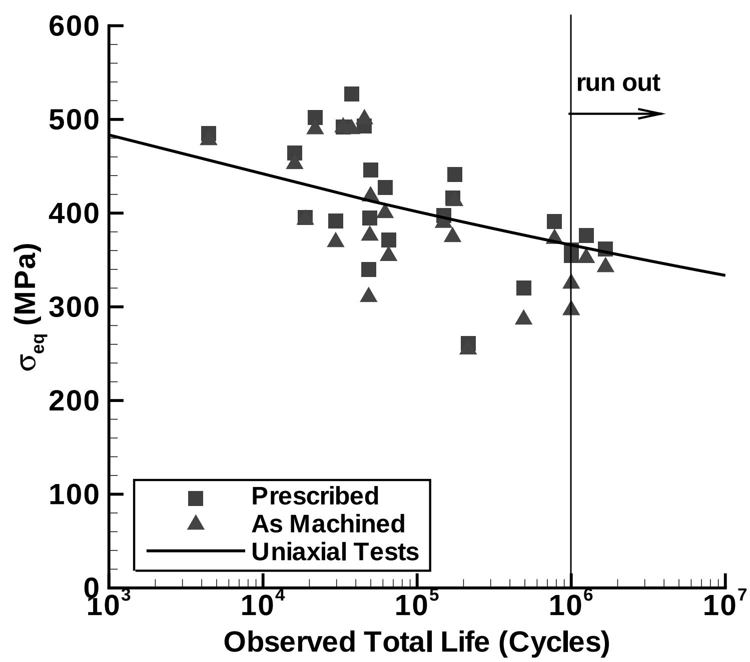

Figure 6.9. Comparison of uniaxial data and fretting data with different lifing parameters - σ_{eq} parameter.

Table 6.2. Calculated nucleation life parameters and estimated propagation lives for fretting tests

Expt. No.	Prescribed Profile SOC	FIN (MPa)	CCB (MPa)	σ_{eq} (MPa)	As machined Profile SOC	FIN (MPa)	CCB (MPa)	σ_{eq} (MPa)	Prop. life (cycles)
HTFF04	0.0088	660	5.05	441	0.0079	632	4.48	413	3105
HTFF05	0.0062	590	3.83	416	0.0056	555	3.29	375	3740
HTFF06	0.0073	628	4.07	427	0.0065	600	3.67	400	7205
HTFF07	0.0049	466	3.02	320	0.0044	415	2.33	287	7767
HTFF08	0.0072	613	4.10	395	0.0072	611	4.07	393	5019
HTFF09	0.012	779	4.77	464	0.0111	751	4.54	453	7965
HTFF10	0.0147	895	4.83	502	0.0138	862	4.63	490	8307
HTFF11	0.0156	957	4.19	493	0.0161	976	4.26	500	79470
HTFF12	0.0095	675	3.98	395	0.009	658	3.70	376	81325
HTFF13	0.0089	640	3.91	391	0.008	611	3.67	373	75824
HTFF14	0.0183	1017	5.95	527	0.0156	916	5.32	490	5404
HTFF15	0.0095	658	3.97	392	0.0083	620	3.65	369	74928
HTFF16	0.0153	885	5.41	485	0.0142	842	5.32	478	6469
HTFF17	0.0106	704	4.01	398	0.01	680	3.93	390	78547
HTFF18	0.0081	626	3.27	360	0.0068	576	2.81	325	213029
HTFF19	0.0044	451	2.09	261	0.0043	435	1.93	255	207290
HTFF20	0.0171	991	5.13	492	0.0172	990	5.19	492	19140
HTFF21	0.0068	579	3.33	355	0.0056	506	2.54	297	124437
HTFF22	0.0072	597	3.39	361	0.0068	579	3.07	342	129460
HTFF23	0.0067	584	3.46	340	0.0061	555	3.10	311	68827
HTFF24	0.0118	768	4.12	446	0.0104	717	3.70	418	34173
HTFF25	0.0084	633	3.60	376	0.0074	601	3.18	352	117158
HTFF26	0.0081	611	3.93	371	0.0075	591	3.76	354	36753

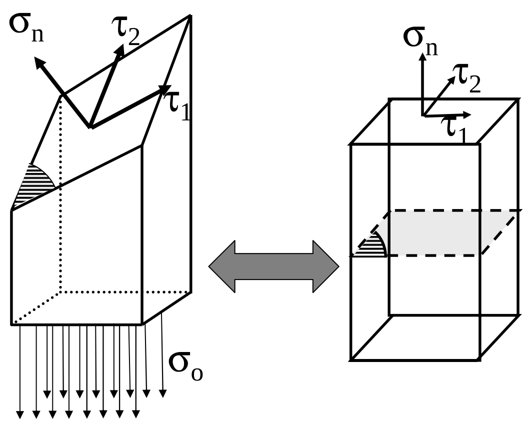

Figure 6.10. Schematic of the assumptions made during propagation analysis. The stresses resolved along and perpendicular to the plane of fracture were assumed to be applied on a specimen with crack perpendicular to its axis.

and starts propagating along <1 1 1> when it is about 250 μm in length. There is a transition region between the two phases when the crack is propagating along intermediate planes. Once the crack reaches the size of 250 μm, it seems to propagate along <1 1 1> plane and fails along the same plane. The crack front appears similar to a corner crack. While a well characterized propagation analysis involves adhering to the three-dimensional characteristics of the crack and is a complex problem, certain assumptions were made to simplify the analysis during this study. The crack was assumed to propagate only along <1 1 1> plane and initial crack size was assumed to be 250 μm. The bulk stress applied to the specimen was resolved in the direction normal to the plane and in two mutually perpendicular directions along the plane. These resolved stresses were assumed to be appiled on a specimen of rectangular cross section with crack perpendicular to the axis of the specimen as shown in the figure 6.10. Stress intensity factor for application of normal stress on a specimen with corner crack (elliptical) was obtained from Anderson (1994).

$$K_I = \sigma_n F \sqrt{\frac{\pi a}{Q}} \tag{6.10}$$

where

$$F = \left[M_1 + M_2 \left(\frac{a}{t}\right)^2 + M_3 \left(\frac{a}{t}\right)^4 \right] g_1 g_2 f_\phi f_w \tag{6.11}$$

$$Q = 1 + 1.464 \left(\frac{a}{c}\right)^{1.65} \tag{6.12}$$

$$M_1 = 1.08 - 0.03 \left(\frac{a}{c}\right) \tag{6.13}$$

$$M_2 = -0.44 + \frac{1.06}{0.3 + \frac{a}{c}} \tag{6.14}$$

$$M_3 = -0.5 + 0.25 \left(\frac{a}{c}\right) + 14.8 \left(1 - \frac{a}{c}\right)^{15} \tag{6.15}$$

$$g_1 = 1 + \left[0.08 + 0.4 \left(\frac{a}{t}\right)^2\right] (1 - \sin\phi)^3 \tag{6.16}$$

$$g_2 = 1 + \left[0.08 + 0.15 \left(\frac{a}{t}\right)^2\right] (1 - \cos\phi)^3 \tag{6.17}$$

$$f_\phi = \left[\left(\frac{a}{c}\right)^2 \cos^2\phi + \sin^2\phi\right]^{1/4} \tag{6.18}$$

$$f_w = \left[\sec\left(\frac{\pi c}{2W}\sqrt{\frac{a}{t}}\right)\right]^{1/2} \tag{6.19}$$

Stress intensity factors for application of shear stress on a specimen with corner crack (elliptical) were obtained from stress intensity factor handbook (Murakami 1987) (Figure 6.11).

Telesman & Ghosn (1996) discuss the application of an octahedral crack driving parameter ΔK_{oct} for obtaining crack growth curve for simple fatigue tests involving the same material under similar bulk loading conditions with cracks propagating along the <1 1 1> plane 6.12. The parameter is defined as

$$\Delta K_{oct} = \sqrt{(\Delta K_I)^2 + (\Delta K_{II})^2 + (\Delta K_{II})^2} \tag{6.20}$$

Parameter ΔK_{oct} was used for the propagation analysis using the crack propagation curve generated by Telesman & Ghosn (1996). Contact stresses have no effect on propagation since the initial crack length is large enough for the steep contact stress gradients to die down. Propagation lives driven by bulk stresses were obtained for each of the experiments and are listed in Table 6.2. Predicted total life, taken as sum of nucleation lives predicted by various damage parameters and propagation lives evaluated from fracture mechanics, was compared against failure lives observed

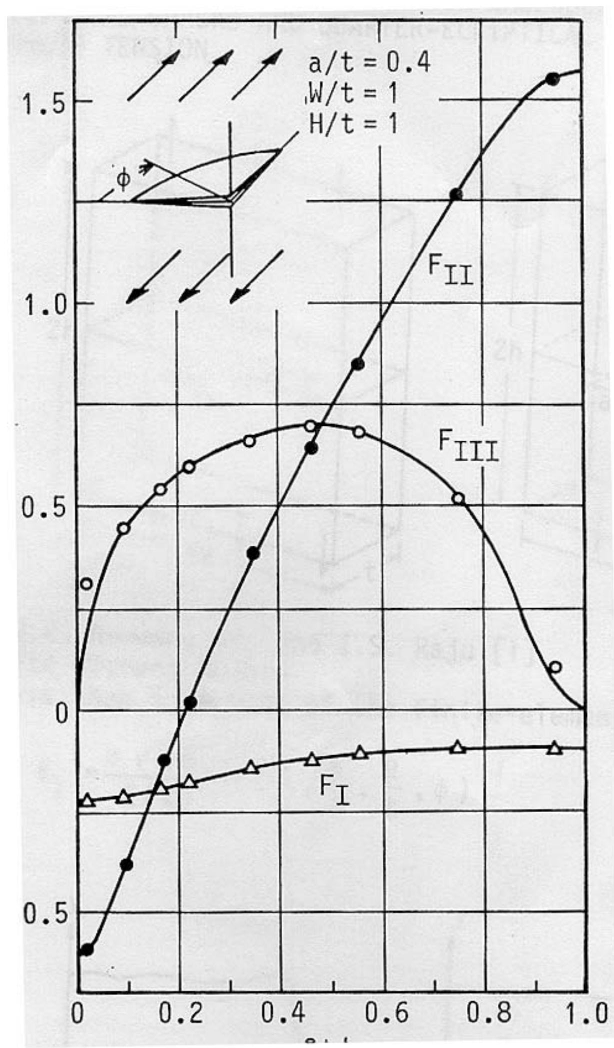

Figure 6.11. Stress intensity factors for corner cracks with remote shear stress. The graph has been reproduced from Murakami (1987)

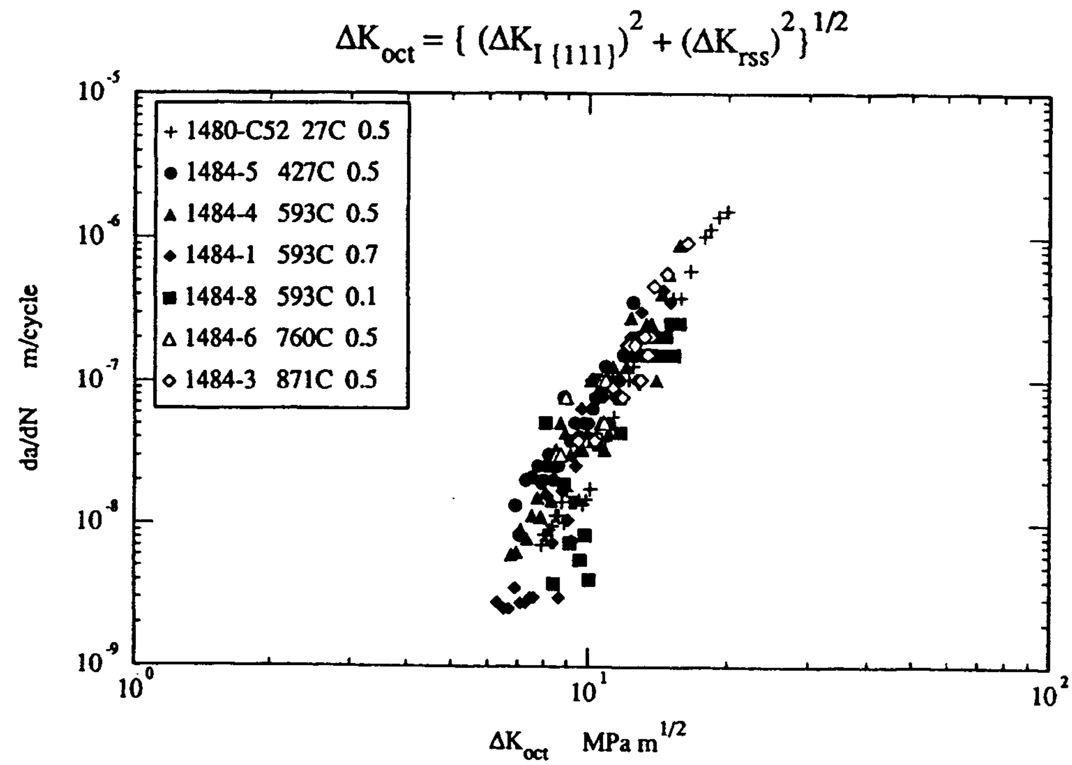

Figure 6.12. Octahedral fatigue crack growth data in terms of ΔK_{oct} parameter. The graph has been reproduced from Telesman & Ghosn (1996).

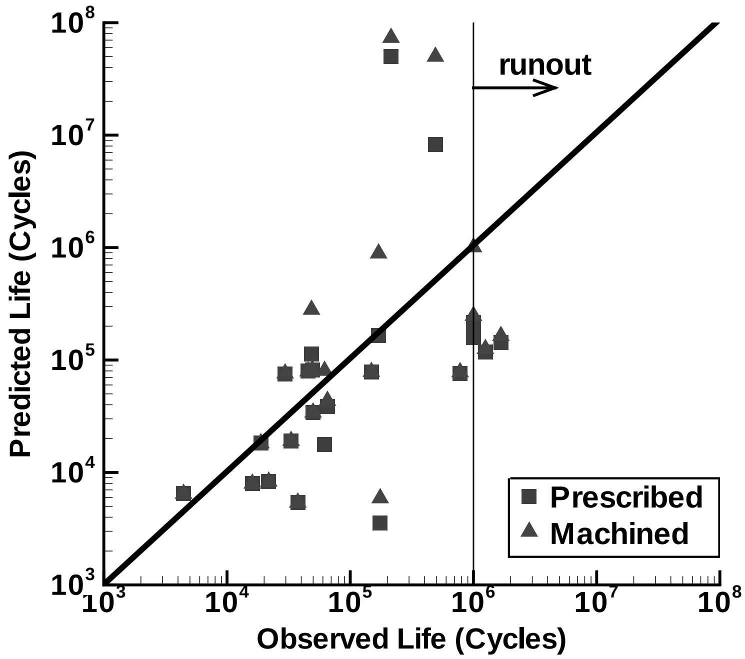

Figure 6.13. Comparison of predicted total life with experimentally observed failure life - Socie's parameter.

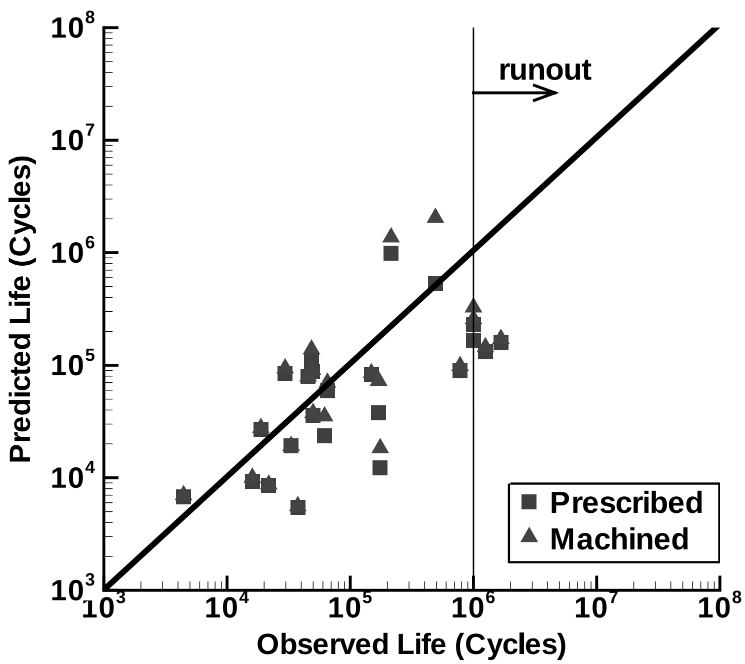

Figure 6.14. Comparison of predicted total life with experimentally observed failure life - Findley's parameter.

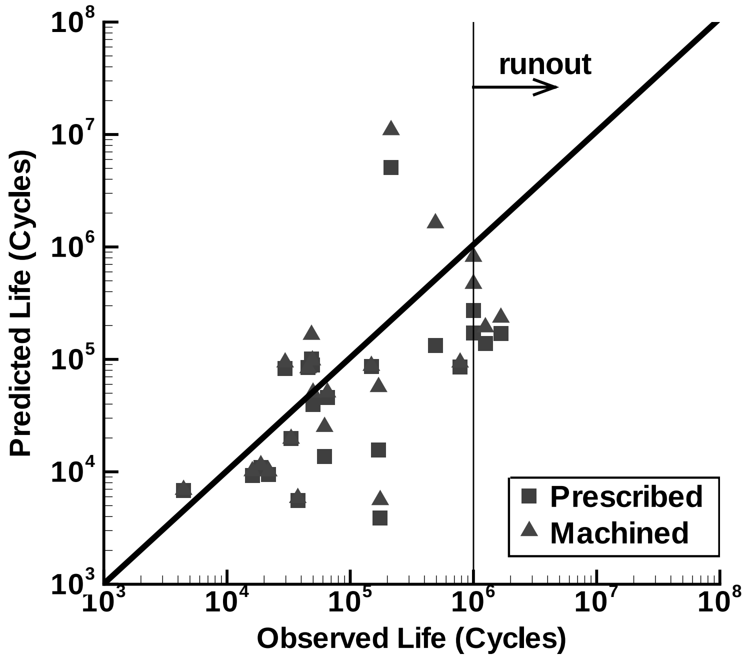

Figure 6.15. Comparison of predicted total life with experimentally observed failure life - CCB parameter.

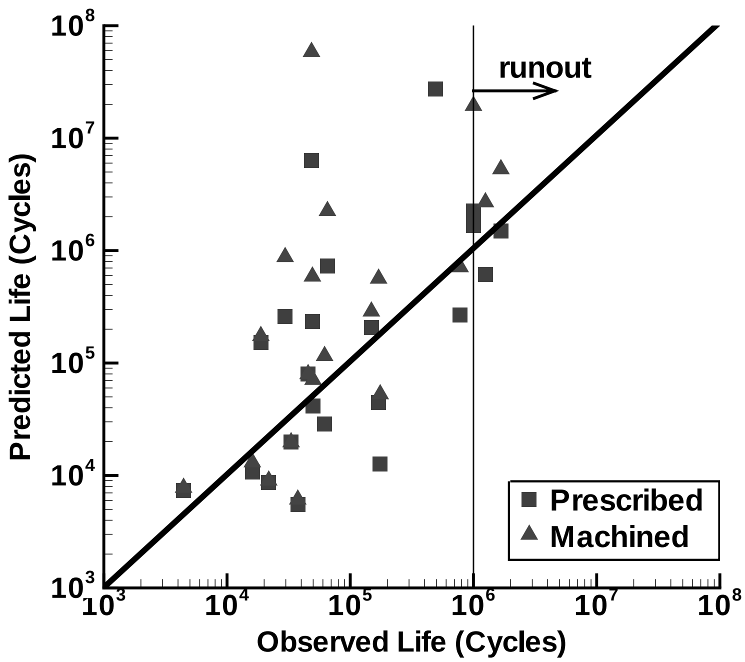

Figure 6.16. Comparison of predicted total life with experimentally observed failure life - σ_{eq} parameter.

during experiments. From figures 6.13 - 6.16, it is observed that Findley parameter and Chu-Conle-Bonnen parameters give the best prediction results among different parameters.

7. Conclusion and Future Work

An experimental setup capable of performing fretting fatigue experiments was designed, built and characterized. It was used to measure fretting fatigue lives for IN100 in contact with single crystal nickel for a range of loads. Measured lives were compared to total life prediction based on a combination of multiaxial fatigue nucleation and fatigue crack growth. Comparisons between predicted and measured lives gives confidence to the notion that conventional fatigue lifing tools can be used to assess fretting fatigue lives.

Future work includes characterization of the effect of surface integrity enhancements on fretting fatigue as well as the examination of mission loading profiles.

LIST OF REFERENCES

LIST OF REFERENCES

Anderson, T. L. (1994), *Fracture Mechanics : Fundamentals and Applications*, CRC Press, New York.

Arakere, N. K. & Swanson, G. (2001), 'Fretting stresses in single crystal superalloy turbine blade attachments', *Journal of Tribology* **123**, 413–423.

Attia, M. H. (1992), Current practice and future prospects for standardization, *in* 'Standardization of Fretting Fatigue Test Methods and Equipment', ASTM, Philadelphia, pp. 263–275.

Bannantine, J. A., Comer, J. J. & Handrock, J. L. (1990), *Fundamentals of Metal Fatigue Analysis*, Prentice Hall, Englewood Cliffs, New Jersey.

Batdorf, S. B. & Heinisch, H. L. (1978), 'Weakest link theory reformulated for arbitrary failure criterion', *Journal of the American Ceramic Society* **61**(7-8), 355–358.

Braun, A. A. (1994), A historical overview and discussion of computer- aided materials testing, 'Automation in Fatigue and Fracture—ASTM STP 1231', ASTM, pp. 5–17.

Chu, C.-C., Conle, F. A. & Bonnen, J. J. F. (1993), Critical plane approaches for multiaxial fatigue damage assessment, 'Advances in Multiaxial Fatigue-ASTM STP 1191', ASTM, Philadelphia, pp. 7–36.

Ciavarella, M., Hills, D. A. & Monno, G. (1998), 'The influence of rounded edges on indentation by a flat punch', *Proceedings of the Institution of Mechanical Engineers, Part C, Journal of Mechanical Engineering Science* **212**(4), 319–328.

Cunningham, S., Deluca, D. & Haake, F. (1996), 'Crack growth and life prediction in single-crystal nickel superalloys', *United Technologies Corporation/Pratt & Whitney M aterials Engineering, Technical Report*.

Dobromirski, J. M. (1992), Variables of fretting process: Are there 50 of them?, M. H. Attia & R. B. Waterhouse, eds, 'Standardization of Fretting Fatigue: Test Methods and Equipment', ASTM STP 1159, American Society of Testing and Materials, Philadelphia, PA, pp. 60–66.

Doner, M., Bain, K. R. & Adams, J. H. (1982), 'Evaluation of methods for the treatment of mean stress effects on low-cycle fatigue', *Journal of Engineering for Power* **104**, 403–411.

Dundurs, J. & Comninou, M. (1979), 'Some Consequences of the Inequality Conditions in Contact and Crack Problems', *Journal of Elasticity* **9**(1), 71–82.

Eden, E. M., Rose, W. N. & Cunningham, F. L. (1911), 'The endurance of metals', *Proceedings–Institution of Mechanical Engineers* **Parts 3-4**, 831–880.

Edwards, P. R. (1981), The application of fracture mechanics to predicting fretting fatigue, *in* R. B. Waterhouse, ed., 'Fretting Fatigue', Applied Science, London, chapter 3, pp. 67–98.

Endo, K. (1981), Practical observations of initiation and propagation of fretting fatigue cracks, *in* R. B. Waterhouse, ed., 'Fretting Fatigue', Applied Science, London, chapter 5, pp. 127–142.

Endo, K. & Goto, H. (1976), 'Initiation and propagation of fretting fatigue cracks', *Wear* **38**, 311–324.

Erdogan, F. & Gupta, G. D. (1972), 'On the Numerical Solutions of Singular Integral E quations', *Quarterly Journal of Applied Mathematics* **29**(4), 525–534.

Farris, T. N. (1992), 'Mechanics of fretting fatigue tests of contacting dissimilar elastic bodies', *STLE, Tribology Transactions* **35**, 346–352.

Farris, T. N., Murthy, H. & Matlik, J. F. (2003), Fretting fatigue, R. O. Ritchie & Y. Murakami, eds, 'Comprehensive Structural Integrity: Fracture of Materials from Macro to Nano', Vol. 4:Cyclic Loading, Elsevier, Amsterdam, pp. 281–326.

Fatemi, A. & Socie, D. F. (1988), 'A critical plane approach to multiaxial fatigue damage including out-of-phase loading', *Fatigue Fract. Engng. Mater. Struct.* **11**(3), 149–165.

Fellows, L. J., Nowell, D. & Hills, D. A. (1997), 'On the initiation of fretting fatigue cracks', *Wear* **205**, 120–129.

Findley, W. N. (1959), 'A theory for the effect of mean stress on fatigue of metals under combined torsion and axial load or bending', *Journal of Engineering for Industry* pp. 301–307.

Giannakopoulos, A. E., Lindley, T. & Suresh, S. (1998), 'Aspects of equivalence between contact mechanics and fracture mechanics: Theoretical connections and a life prediction methodology for fretting fatigue', *Acta Mater.* **46**(9), 2955–2968.

Giannakopoulos, A., Lindley, T., Suresh, S. & Chenut, C. (2000), 'Similarities of stress concentrations in contact at round punches and fatigue at notches: Implications to fretting fatigue crack initiation', *Fatigue & Fracture of Engineering Materials & Structures* **23**, 561–571.

Gladwell, G. M. L. (1980), *Contact Problems in the Classical Theory of Elast icity*, Sijthoff & Noordhoff, Germantown, Maryland.

Goryacheva, I. G., Murthy, H. & Farris, T. N. (2002), 'Contact problem with partial slip for the inclined punch with rounded edges', *International Journal of Fatigue* **24**(11), 1191–1201.

Harish, G., Szolwinski, M. P., Farris, T. N. & Sakagami, T. (2000), Evaluation of fretting stresses through full-field temperature measurements, D. W. Hoeppner, V. Chandrasekaran & C. B. Elliott, eds, 'Fretting Fatigue: Current Technology and Practices, STP 1367', American Society for Testing and Materials, West Conshohocken, PA, pp. 423–435.

Hattori, T., Nakamura, M., Sakata, H. & Watanabe, T. (1988), 'Fretting fatigue analysis using fracture mechanics', *JSME International Journal, Series I* **31**(1), 100–107.

Hills, D. A. (1994), 'Mechanics of fretting fatigue', *Wear* **175**, 107–113.

Hills, D. A. & Nowell, D. (1994), *Mechanics of Fretting Fatigue*, Kluwer Academic Publishers, The Netherlands.

Hills, D. A., Nowell, D. & O'Connor, J. J. (1988), 'On the mechanics of fretting fatigue', *Wear* **125**, 129–146.

Hills, D. A., Nowell, D. & Sackfield, A. (1993), *Mechanics of Elastic Contacts*, Butterworth-Heinemann Ltd, Oxford, Great Britain.

Hurricks, P. L. (1970), 'Mechanism of fretting', *Wear* **15**, 389–409.

Jäger, J. (1997), 'Half-planes without coupling under contact loading', *Archive of Applied Mechanics* **67**, 247–259.

Kalb, B. J. (1991), Friction stresses between blade and disk dovetail possible case of numerous dovetail problems, *in* 'USAF Structural Integrity Conference'.

Karpenko, L. N. (1966), 'Approximate Solution of a Singular Integral Equation by means of Jacobi Polynomials', *Journal of Applied Mathematics and Mechanics* **30**(3), 668–675.

Kondoh, K. & Mutoh, Y. (2000), Crack behavior in the early stage of fretting fatigue fracture, D. W. Hoeppner, V. Chandrasekaran & C. Elliott, eds, 'Fretting Fatigue: Current Technology and Practices, STP 1367', ASTM, West Conshohocken, PA, pp. 282–292.

Kurtz, R., Farris, T. & Sun, C. (1994), 'The Numerical Solution of Cauchy Singular Integra l Equations with Application to Fracture', *International Journal of Fracture* **66**, 139–154.

Lekhnitskii, S. G. (1981), *Theory of Elasticity of an Anisotropic Body*, Mir Publishers, Moscow, U. S. S. R.

Lindley, T. (1997), 'Fretting fatigue in engineering alloys', *International Journal of Fatigue* **19**(1), S39–S49.

McDowell, J. R. (1953), Fretting corrosion tendencies of several combinations of materials, 'ASTM STP 144: Symposium on Fretting Corrosion', Philadelphia, PA, pp. 24–39.

McVeigh, P. A., Harish, G., Farris, T. N. & Szolwinski, M. P. (1999), 'Modeling interfacial conditions in nominally flat contacts for application to fretting fatigue of turbine engine components', *International Journal of Fatigue* **S1**, 157–165.

Mindlin, R. D. (1949), 'Compliance of elastic bodies in contact', *Journal of Applied Mechanics* **16**(3), 259–268.

Murakami, Y., ed. (1987), *Stress Intensity Factors Handbook*, Oxford: Pergamon Press.

Murthy, H., Harish, G. & Farris, T. (2003), 'Efficient modeling of fretting of blade/disk contacts including load history effects', *Journal of Tribology* **125**, 1–9.

Murthy, H., Harish, G. & Farris, T. N. (2000), Influence of contact profile on fretting crack nucleation in a titanium alloy, *in* 'Collection of Technical Papers - AIAA/ASME/ASCE/AHS/ASC Structures, Structural Dynam ics and Materials Conference', Vol. 2(1), AIAA, pp. 1326–1333.

Murthy, H., Rajeev, P., Farris, T. N. & Slavik, D. C. (2001), 'Fretting fatigue of Ti-6Al-4V subjected to blade/disk contact loading', *Developments in Fracture Mechanics for the New Century, 50th Anniversary of Japan Society of Materials Science* pp. 41–48.

Muskhelishvili, N. I. (1953), *Singular Integral Equations*, Groningen, P. Noordhoff.

Nishioka, K. & Hirakawa, K. (1969), 'Fundamental investigations of fretting fatigue, part 3', *Bulletin of JSME* **12**(51), 397–407.

Nowell, D. & Hills, D. A. (1987), 'Mechanics of fretting fatigue tests', *International Journal of Mechanical Sciences* **29**(5), 355–365.

Petiot, C., Vincent, L., Dang Van, K., Maouche, N., Foulquier, J. & Journet, B. (1995), 'An analysis of fretting–fatigue failure combined with numerical calculations to predict crack nucleation', *Wear* **181-183**, 101–111.

Rajeev, P. & Farris, T. (2002), 'Numerical analysis of fretting contacts of dissimilar isotropic and anisotropic materials', *Journal of Strain Analysis* **37**(6), 503–517.

Ruiz, C., Boddington, P. H. B. & Chen, K. C. (1984), 'An investigation of fatigue and fretting in a dovetail joint', *Experimental Mechanics* **24**(3), 208–217.

Schenk, B., Brehm, P., J., Menon, M., N., Tucker, W. T. & Peralta, A. D. (2000), 'A new probabilistic approach for accurate fatigue data analysis of ceramic materials', *Journal of Engineering for Gas Turbines and Power-Transactions of the ASME* **122**(4), 637–645.

Socie, D. (1987), 'Multiaxial fatigue damage models', *Journal of Engineering Materials and Technology* **109**, 292–298.

Spence, D. A. (1973), 'An Eigenvalue Problem for Elastic Contact with Fi nite Friction', *Proceedings of the Cambridge Philosophical Society* **73**, 249–268.

Szolwinski, M. P. & Farris, T. N. (1996), 'Mechanics of fretting fatigue crack nucleation', *Wear* **198**, 93–107.

Szolwinski, M. P. & Farris, T. N. (1998), 'Observation, analysis and prediction of fretting fatigue in 2024-t351 aluminum alloy', *Wear* **221**, 24–36.

Telesman, J. & Ghosn, L. J. (1996), Crack growth and life prediction in single-crystal nickel superalloys, Technical Report WL-TR-94-4090, Materials Directorate, Wright Laboratory, Wright-Patterson AFB, OH.

Ting, T. C. T. (1996), *Anisotropic Elasticity: Theory and Applications*, Oxford University Press, New York.

Tomlinson, G. A. (1927), The rusting of steel surfaces in contact, *in* 'Proc. Royal Soc., Series A', Vol. 115, pp. 472– 483.

Waterhouse, R. B. (1981), Fretting fatigue in aqueous electrolytes, *in* 'Fretting Fatigue', Applied Science, London, chapter 7, pp. 159–176.

Waterhouse, R. B. & Taylor, D. E. (1971), 'The initiation of fatigue cracks in a 0.7% carbon steel by fretting', *Wear* **17**, 139–147.

Waterhouse, R. B., ed. (1972), *Fretting Corrosion*, Pergamon, Oxford.

VITA

Murthy N. Haradanahalli (H.S.N. Murthy) was born and brought up in the city of Bangalore, India. He had his primary and secondary education in Womens Peace League Composite School, Bangalore. He finished his pre-university education (equivalent of 12th grade) from the M.E.S. college of arts, science & commerce (Bangalore) in 1993. He studied medicine for a year at Bangalore Medical College. He then shifted to Indian Institute of Technology Madras, Chennai (India) to pursue Bachelor of Technology degree in Aerospace Engineering. He graduated in August, 1998 and joined the school of Aeronautics and Astronautics at Purdue University to pursue Master of Science degree which he completed in December, 2000. He has been working on his PhD since then. After graduation he plans to join as faculty in one of the Universities in India.